technologies

Article

A Fuzzy-Driven Synthesis: MiFREN-Optimized Magnetic Biochar Nanocomposite from Agricultural Waste for Sustainable Arsenic Water Remediation †

Sasirot Khamkure [1,*], Chidentree Treesatayapun [2], Victoria Bustos-Terrones [3], Lourdes Díaz Jiménez [4], Daniella-Esperanza Pacheco-Catalán [5], Audberto Reyes-Rosas [6], Prócoro Gamero-Melo [4], Alejandro Zermeño-González [7], Nakorn Tippayawong [8] and Patiroop Pholchan [9,*]

1 Irrigation and Drainage Department, Secretaría de Ciencia, Humanidades, Tecnología e Innovación (SECIHTI)-Universidad Autónoma Agraria Antonio Narro, Saltillo 25315, Coahuila, Mexico
2 Departament of Robotic and Advanced Manufacturing, Cinvestav Saltillo, Ramos Arizpe 25900, Coahuila, Mexico; chidentree@cinvestav.edu.mx
3 Environmental Engineering and Sustainability Research Laboratory, Universidad Politécnica del Estado de Morelos, Jiutepec 62550, Morelos, Mexico; vbustos@upemor.edu.mx
4 Sustainability of Natural Resources and Energy, Cinvestav Saltillo, Ramos Arizpe 25900, Coahuila, Mexico; lourdes.diaz@cinvestav.edu.mx (L.D.J.); procoro.gamero@cinvestav.edu.mx (P.G.-M.)
5 Renewable Energy Unit, Yucatan Scientific Research Center, Merida 97302, Yucatan, Mexico; dpacheco@cicy.mx
6 Department of Bioscience and Agrotechnology, Centro de Investigación en Química Aplicada, Saltillo 25294, Coahuila, Mexico; audberto.reyes@ciqa.edu.mx
7 Irrigation and Drainage Department, Universidad Autónoma Agraria Antonio Narro, Saltillo 25315, Coahuila, Mexico; azermeno@uaaan.edu.mx
8 Department of Mechanical Engineering, Faculty of Engineering, Chiang Mai University, Chiang Mai 50200, Thailand; nakorn.t@cmu.ac.th
9 Department of Environmental Engineering, Faculty of Engineering, Chiang Mai University, Chiang Mai 50200, Thailand
* Correspondence: skhamkure@secihti.mx (S.K.); patiroop@eng.cmu.ac.th (P.P.)
† This part is an extended version of the paper published in 7th International Conference on ICT Integration in Technical Education (ETLTC2025), University of Aizu, Aizuwakamatsu, Japan, 20–26 January 2025.

Abstract

Arsenic contamination demands innovative, sustainable remediation. This study presents a fuzzy approach for synthesizing a magnetic biochar nanocomposite from pecan shell agricultural waste for efficient arsenic removal. Using a Multi-Input Fuzzy Rules Emulated Network (MiFREN), a systematic investigation of the synthesis process revealed that precursor type (biochar), Fe:precursor ratio (1:1), and iron salt type were the most significant parameters governing material crystallinity and adsorption performance, while particle size and N_2 atmosphere had a minimal effect. The MiFREN-identified optimal material, the magnetic biochar composite (FS7), achieved > 90% arsenic removal, outperforming the least efficient sample by 50.61%. Kinetic analysis confirmed chemisorption on a heterogeneous surface (q_e = 12.74 mg/g). Regeneration studies using 0.1 M NaOH demonstrated high stability, with FS7 retaining > 70% removal capacity over six cycles. Desorption occurs via ion exchange and electrostatic repulsion, with post-use analysis confirming structural integrity and resistance to oxidation. Application to real groundwater from the La Laguna region proved highly effective; FS7 maintained selectivity despite competing ions like Na^+, Cl^-, and SO_4^{2-}. By integrating AI-driven optimization with reusability and real contaminated water, this research establishes a scalable framework for transforming agricultural waste into a high-performance adsorbent, supporting global Clean Water and Sanitation goals.

Academic Editor: Miklas Scholz

Received: 4 December 2025
Revised: 23 December 2025
Accepted: 4 January 2026
Published: 7 January 2026

Keywords: adsorption; arsenic removal; fuzzy decision network; magnetite composite biochar; performance optimization

1. Introduction

Groundwater arsenic contamination critically undermines progress toward the United Nations Sustainable Development Goal 6 (SDG 6) and endangers millions of lives, with severe hotspots in South Asia and the Americas frequently exceeding concentrations of 500 μg/L [1]. Regulatory inertia exacerbates this ongoing crisis, as numerous authorities uphold less stringent standards rather than adopting the World Health Organization (WHO) 10 μg/L guideline. For example, extreme levels have been recorded in the Ganges River alluvial deposits and the Bengal Delta Plain (up to 2 mg/L) [2], and in Thailand, where groundwater concentrations have reached 5 mg/L [3]. Similar high-level contamination has been documented in Pakistan (2.58 mg/L) and Vietnam (3.05 mg/L) [3]. In Latin America, concentrations as high as 3.81 mg/L have been reported in Argentina [4]. In response, the development of sustainable, efficient, and practical water treatment technologies is paramount. Adsorption has emerged as a frontline remediation strategy, with biochar—a porous carbonaceous material derived from biomass waste—gaining prominence as a low-cost and sustainable adsorbent [5–8]. The conversion of agricultural residues, such as pecan nutshells, into biochar not only addresses water pollution but also contributes to a circular economy by valorizing waste streams, thereby supporting broader environmental sustainability goals [9,10].

The performance of biochar is intrinsically linked to its physicochemical properties, which are governed by feedstock selection and synthesis conditions [7,11,12]. To enhance its functionality and facilitate practical application, the integration of magnetic nanoparticles, particularly magnetite (Fe_3O_4), has proven highly effective [13–16]. This modification creates magnetic biochar composites that combine the high adsorption capacity of biochar with the facile separation capability provided by magnetism, significantly improving the efficiency and cost-effectiveness of water treatment processes [5,6].

Biochar is a highly promising adsorbent for waterborne microcontaminants at scale. To bridge the gap from lab research to real-world use, its practical application requires key developments, including pilot-scale validation, stability assessments, and studies on competing ion effects [17]. In this process, artificial intelligence (AI) is emerging as a powerful tool to accelerate and optimize the design of such environmental remediation materials. Algorithms such as Random Forest and MiFREN predict and optimize synthesis parameters, minimizing the need for extensive experimentation and streamlining the development of efficient adsorbents. AI-driven frameworks employing ML algorithms (e.g., Random Forest, Gradient Boosting) are proving highly effective for modeling of engineered biochar for soil and water contaminant removal. An ML-based framework has been reported to optimize the key biochar adsorbents' properties to adsorb antibiotics [18], phosphorus [19] and heavy metals [20]. Through predictive modeling, these tools optimize synthesis parameters, which substantially reduce the number of experiments and lead to significant reductions in development cost and time [21].

However, the synthesis of high-performance magnetic biochar is a complex, multi-parameter process. Variables such as precursor type (raw biomass vs. biochar), particle size, iron-to-precursor ratio, and synthesis atmosphere interact in non-linear ways, making traditional one-variable-at-a-time optimization methods inadequate [22,23]. This complexity creates a pressing need for performance enhancement frameworks that can navigate these uncertain and interdependent relationships to design superior adsorbents. More-

over, arsenic adsorption studies consistently demonstrate that initial arsenic concentration, pH, adsorbent dose, and experimental conditions significantly influence removal efficiency [24,25]. Multiple studies across different adsorbent materials (e.g., activated carbon, graphene oxide, iron oxides) confirm the critical roles of these parameters [26–29].

This work develops magnetic biochar adsorbents from pecan shells, an agricultural residue. The material is synthesized by pyrolysis and subsequent incorporation of magnetite (Fe_3O_4) nanoparticles, a strategy that combines sustainability with magnetic functionality to facilitate its recovery. The study focused on As(V) due to its direct rele-vance to applied water treatment. In practice, As(III) is routinely pre-oxidized to As(V) using standard chemical methods because the pentavalent form is adsorbed far more efficiently by materials like magnetic biochar [1]. Evaluating As(V) thus directly measures the adsorbent's performance under the most effective and common remediation conditions.

Herein, fuzzy logic emerges as a compelling technological solution for environmental modeling. Specifically, Fuzzy Decision Networks (FDNs), such as the Multi-Input Fuzzy Rules Emulated Network (MiFREN), are strategically implemented to model complex, non-linear systems where the limitations of traditional, deterministic mathematical models become evident [22]. MiFREN stands out as uniquely well-suited to this study because its hybrid architecture effectively addresses the critical need for both predictive power and model transparency in practical remediation applications. By integrating the high-fidelity mapping of neural networks with the linguistic reasoning of fuzzy systems, MiFREN moves beyond the 'black box' limitation of strictly data-driven approaches. This allows it to emulate human-like reasoning, handle the inherent imprecision in experimental data, and, crucially, reveal the explicit rules governing material behavior [23,24]. The ability of MiFREN to construct robust performance indices and identify most effective synthesis pathways through interpretable logic represents a significant advancement in environmental materials science, establishing a more predictive and strategically design-driven paradigm [25].

Consequently, this study introduces a novel, fuzzy-framework for the synthesis and optimization of a magnetic biochar nanocomposite derived from pecan nutshells for arsenic removal. We systematically investigated the impact of key synthesis parameters and employed the MiFREN architecture specifically to model, assess, and optimize the adsorption performance at the studied conditions. The primary objectives of this work are threefold: (1) to successfully valorize agricultural waste into a high-value magnetic adsorbent; (2) to precisely decipher the complex, non-linear relationships between synthesis variables and arsenic removal efficiency, utilizing the interpretable rules offered by MiFREN; and (3) to empirically demonstrate the potential of this advanced AI-driven fuzzy logic approach to reliably guide the sustainable design and application of next-generation water treatment materials.

This study represents a significant advancement by being the first to employ the interpretable MiFREN architecture for the coupled synergistic enhancement of magnetic biochar synthesis and subsequent arsenic adsorption performance. Unlike prior studies that rely on empirical or 'black-box' modeling techniques, this work delivers a transparent, rule-based computational framework that allows for the direct linkage between synthesis parameters and real-world adsorption efficiency, offering a robust tool for designing sustainable water treatment systems. The results of this study are obtained through a four-part methodology focused on the synthesis, characterization, arsenic adsorption performance, and computational optimization of the magnetic biochar nanocomposite. Key synthesis parameters were systematically varied, including precursor type, particle size, Fe:Precursor ratio, and synthesis atmosphere (N_2 gas vs. air). The resulting composites were tested in batch adsorption experiments across five different conditions (EXP I–V). Finally, the experimental data were

used to construct the MiFREN network, allowing for the modeling of complex, non-linear relationships and the subsequent refinement of the synthesis pathway for superior arsenic removal. Based on this approach, the key hypothesis tested in this work is that the MiFREN model can accurately and reliably predict the optimal combination of material synthesis and operational parameters for maximizing arsenic removal, thereby demonstrating its superior utility over conventional modeling approaches in materials science.

2. Materials and Methods

2.1. Synthesis of Magnetic Biochar Composites via Co-Precipitation

Pecan nutshell-derived adsorbents were synthesized in sequential steps. First, raw pecan shells were cleaned with deionized water, dried at 60 °C for 24 h, ground, and sieved into two particle size ranges (0.105–0.18 mm and 0.38–0.7 mm). The powder was pyrolyzed at 500 °C for 1 h under a nitrogen atmosphere to produce biochar. This pyrolysis temperature was selected based on literature precedents [16,30,31], as it balances carbon yield with surface functional group development.

Magnetic biochar composites were synthesized via co-precipitation. For magnetic modification, $FeCl_3 \cdot 6H_2O$ (0.1 mol) and $FeSO_4 \cdot 7H_2O$ (0.05 mol) were dissolved in 600 mL of water. NaOH was added dropwise under vigorous stirring (80 °C, 500 rpm) to adjust the pH to 10. Pecan biomass (PM) or biochar was then added and stirred for 30 min at 80 °C, either with or without N_2 gas purging. Finally, the resulting magnetic nanocomposites were magnetically separated, washed until neutral, and dried at 60 °C.

This study evaluated the effect of various factors on properties of the adsorbent for arsenic removal, including precursor (biomass and biochar), iron salt ($FeSO_4 \cdot 7H_2O$ and $FeSO_4(NH_4)_2SO_2 \cdot 6H_2O$), particle size (0.10–0.18 mm and 0.38–0.7 mm), Fe:precursor ratio, and N_2 gas.

Ten magnetic composites were synthesized via co-precipitation to evaluate specific experimental parameters. FS1 utilized a unique iron source ($FeCl_3 \cdot 6H_2O$+Mohr's salt), while FS2–FS10 employed a standard $FeCl_3 \cdot 6H_2O$/$FeSO_4 \cdot 7H_2O$ mixture. The effects of biomass particle size were tested under ambient air (FS2, FS3, FS8) and N_2 atmosphere (FS4, FS5, FS6). Additionally, the study assessed the use of biochar as a support (FS7) and varied the Fe:precursor mass ratio from the standard 1:1 (FS1–FS8) to 1:2 (FS9) and 1:3 (FS10).

2.2. Characterization

The synthesized magnetic biochar composites were characterized to determine their crystallinity, surface morphology, and textural properties. X-Ray Diffraction (XRD) analysis was performed to identify the crystalline phases present and assess their crystallinity. Measurements were carried out using a Bruker diffractometer (D8 ADVANCE, Karlsruhe, Germany) equipped with a Göbel mirror and a Cu-Kα radiation source. Data were collected over a 2θ range of 20° to 80°. Surface morphology and elemental composition were examined using a Philips XL30 Environmental Scanning Electron Microscopy (ESEM) (Eindhoven, the Netherlands). The microscope was equipped with an Energy Dispersive X-ray Spectroscopy (EDS) system for elemental analysis.

Textural properties, including specific surface area, pore volume, and pore size distribution, were determined by nitrogen physisorption at 77 K using a Quantachrome Instruments analyzer (NOVA touch 2LX) (Boynton Beach, FL, USA). The specific surface area was calculated using the Brunauer-Emmett-Teller (BET) method, while the pore size distribution was derived from the adsorption isotherms using the Quenched Solid Density Functional Theory (QSDFT) model for carbon slit pores.

2.3. Preliminary Arsenic Adsorption Evaluation

Batch adsorption experiments were conducted as a preliminary screening to evaluate the arsenic removal performance of the synthesized adsorbents (FS1–FS10) and raw pecan nutshell (PM). The objective of these tests (EXP I–V) was to identify the most versatile and robust composite by challenging the materials across a spectrum of initial concentrations (1, 5, or 10 mg/L), pH levels, and adsorbent doses. The arsenic concentrations of 1, 5, and 10 mg/L were selected to reflect the elevated levels commonly found in global groundwater contamination hotspots [1].

To maximize the scope of the study, the adsorbents were tested under five distinct experimental conditions representing various stress levels. While these screening tests were performed as single runs to expedite the selection of the lead adsorbent, the high degree of internal consistency observed across the diverse experimental matrix supports the reliability of the identified trends. Following this selection process, systematic studies were performed for pH (3, 4, or 5), adsorbent dose (1 or 2 g/L), and agitation speed (100 or 150 rpm) to isolate and quantify the impact of each individual parameter.

The specific parameters for each condition are detailed below:

- EXP I: As 1 mg/L, 2 g/L adsorbent (50 mg/25 mL), 24 h, agitation at 100 rpm, pH 3;
- EXP II: As 1 mg/L, 2 g/L adsorbent (50 mg/25 mL), 24 h, agitation at 100 rpm, pH 4;
- EXP III: As 5 mg/L, 2 g/L adsorbent, 24 h, agitation at 150 rpm, pH 3;
- EXP IV: As 10 mg/L, 1 g/L adsorbent, 24 h, agitation at 150 rpm, pH 3;
- EXP V: As 10 mg/L, 1 g/L adsorbent, 24 h, agitation at 150 rpm, pH 5.

Adsorption performance was evaluated using arsenic removal efficiency (%), which was determined as:

$$\% \text{ As Removal} = [(C_0 - C_e)/C_0] \times 100 \quad (1)$$

where C_0 and C_e are the initial and equilibrium arsenic concentrations (mg/L), respectively.

2.4. Analysis of Fuzzy Decision Network

The proposed method for analyzing the performance of the Fuzzy Decision Network involved constructing the MiFREN based on experimental data. This process began with defining the input parameters, such as normalized removal quality q_{eN}, and designing membership functions μ_{L-Z} to represent the fuzzified inputs. The architecture of MiFREN integrates weight vectors, w, which were tailored to experimental setups, ensuring adaptability to varying conditions. The performance index Q_r was formulated as a summation of weighted basis functions, ϕ_j, derived from combinations of membership functions. These basis functions encapsulate the nonlinear interactions between the input parameters, enabling the network to emulate complex decision-making processes.

The computational framework was implemented using unity functions for simplicity, while simultaneously ensuring generality in the derivation of ϕ_j. Experimental results were validated by comparing Q_r values across multiple samples, thereby providing insights into the influence of material properties, particle size, and preparation methods on the overall system performance. This analytical approach highlighted the efficacy of MiFREN in modeling nonlinear relationships and tailoring performance in arsenic removal applications.

2.5. Kinetic Adsorption Experiments

The adsorption kinetics of arsenic onto the selected magnetic biochar nanocomposites (FS4, FS7, FS8) were investigated through batch experiments. A stock solution of arsenic (As(V)) with a concentration of 35.99 mg/L was prepared. For each experiment, 150 mL of this solution was placed in a glass vessel, and the pH was adjusted to 3.5 using 0.1 M

HCl or NaOH. A precise adsorbent dose of 300 mg was added to the solution, resulting in a constant concentration of 2 g/L. The mixture was agitated on an orbital shaker at a constant speed of 150 rpm. Samples were withdrawn at predetermined time intervals (10, 20, 30, 60, 120, 240, 360, 480, and 600 min), immediately filtered through a 0.45 µm syringe filter to separate the adsorbent, and the filtrate was preserved for arsenic analysis.

The adsorption capacity at time t (q_t) was calculated using the mass balance equation:

$$q_t = [(C_0 - C_t) \times V]/m \quad (2)$$

where C_t is the concentration at time t (mg/L), V is the solution volume (L), and m is the mass of adsorbent (g).

To elucidate the adsorption mechanism and rate-controlling steps, the experimental data were analyzed using non-linear regression (R software v4.0.3) with three kinetic models: Pseudo-First Order (PFO), Pseudo-Second Order (PSO), and the Elovich model [32]. The goodness-of-fit for each model was evaluated using correlation coefficients (R^2) and root mean square error (RMSE).

2.6. Desorption and Regeneration Studies

To evaluate the stability and economic feasibility of the magnetic biochar nanocomposite, desorption and reusability tests were performed. FS7 was first saturated with arsenic under adsorption kinetic conditions, washed with deionized water, and dried. Desorption efficiency was initially screened using four eluting agents—NaCl (0.1 M), HCl (1 M), NaOH (0.1 and 0.2 M), and KOH (1 and 2 M)—at a solid-to-liquid ratio of 1.5 g/L. The mixtures were agitated for 2–6 h to identify the most effective conditions.

Subsequently, six consecutive adsorption–desorption cycles were conducted to assess reusability. Each cycle involved:

Adsorption: Treatment of arsenic solution at pH 3.0 (2 g/L dose) for 7 h.

Desorption: Exposure to the the best eluant (0.1 M NaOH) for 4 h at 150 RPM.

Regeneration: Washing and pH adjustment to 3.0 to re-activate the adsorbent surface.

The desorption efficiency was calculated as follows [33,34]:

$$\text{Desorption efficiency} = \frac{amount\ of\ metal\ desorbed}{amount\ of\ metal\ ions\ adsorbed} \times 100 \quad (3)$$

To evaluate the chemical and structural of the composite, XRD was performed on both the magnetic biochar (FS7) and the material recovered after adsorption–desorption cycles (FS7-D6).

2.7. Application of FS7 Nanocomposite for Arsenic Remediation in Real Groundwater

The practical efficacy of the FS7 nanocomposite was evaluated using natural groundwater from the Main Aquifer of the La Laguna Region (Torreón, Coahuila, Mexico). The raw water was characterized by an initial As concentration of 0.075 mg/L and a natural pH of 11.37. Batch experiments were conducted by adding 20 mg of FS7 to 10 mL of groundwater (2 g/L dose) in reaction vessels. To identify most favorable remediation window, the solution pH was adjusted to 3.5, 5.0, and 6.0 using 0.1 M HCl. The mixtures were agitated on an orbital shaker for 6 h to reach equilibrium. Post-adsorption, the FS7 particles were isolated via an external magnetic field, and the supernatant was filtered (0.45 µm) for residual arsenic analysis to determine the removal efficiency and equilibrium capacity.

2.8. Analytical Method

The residual arsenic concentration for the preliminary adsorption, kinetic, isotherm, and desorption studies was determined by Inductively Coupled Plasma Optical Emission Spectrometry (ICP-OES) using a PerkinElmer Optima 8300 spectrometer (Shelton, CT, USA). For the study of application with groundwater, arsenic concentration was measured by an ICP-OES Analyzer and Qtegra softwareversion 2.4.1800.192 (iCAP7400 Duo, Thermo Scientific, Waltham, MA, USA).

3. Results

3.1. Impact of Synthesis Parameters on Magnetic Phase Crystallinity

X-ray diffraction (XRD) analysis, as presented in Figure 1, confirmed the successful synthesis of magnetite (Fe_3O_4) nanoparticles within all magnetic biochar composites (FS2–FS10). The analysis is presented alongside the standard reference pattern for Fe_3O_4.

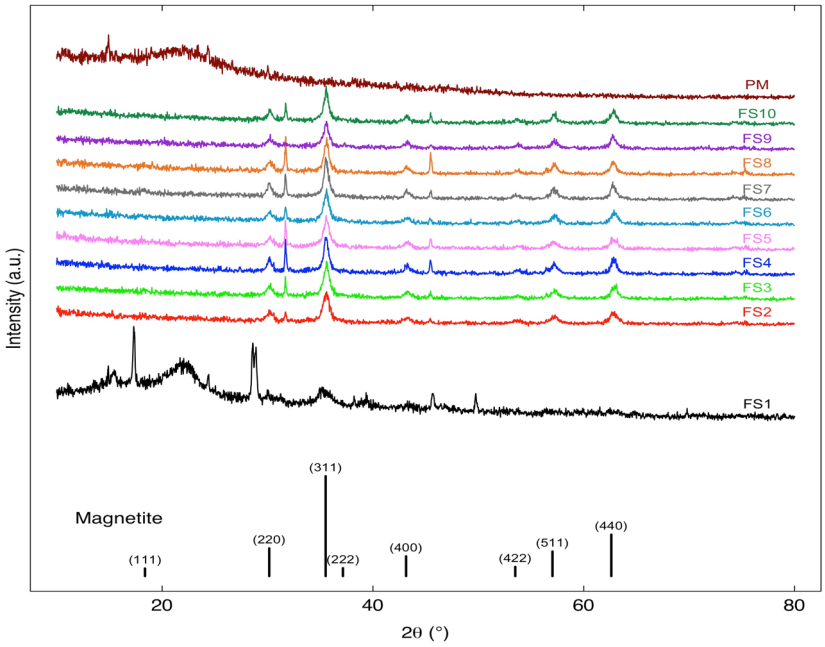

Figure 1. X-ray Diffraction (XRD) Patterns of Raw Pecan Shell Biomass (PM), Magnetic Biochar Composites (FS1–FS10), and Magnetite Reference Standard [14].

The diffractogram of the raw pecan nutshell biomass (PM) exhibits a broad, diffuse hump centered between 2θ ≈ 20° and 25°, which is characteristic of amorphous lignocellulosic materials (cellulose and lignin) with no defined crystalline peaks [35].

For samples FS2 through FS10, the diffractograms display a similar crystalline profile with five characteristic diffraction peaks clearly visible at 2θ values of approximately 30.1°, 35.4°, 43.1°, 57.0°, and 62.6°. These correspond to the (220), (311), (400), (511), and (440) lattice planes, respectively, matching the standard diffraction data for the cubic spinel structure of magnetite (Fe_3O_4) [36,37]. The diffraction peaks for FS2–FS10 are notably broadened, indicating the formation of crystallites in the nanometer range. In contrast, sample FS1 showed distinct sharp peaks at 2θ values of approximately 18°, 20°, and 28°, which do not correspond to the magnetite structure, indicating the method used for FS1 was unsuccessful in forming the target magnetic phase.

The crystallinity and peak intensity of the Fe_3O_4 phase, primarily reflected by the prominent (311) plane, varied systematically with the synthesis parameters [38]. The biochar-derived composite (FS7) exhibited sharper and more intense Fe_3O_4 peaks compared to biomass-derived counterparts (e.g., FS2, FS4), suggesting improved crystallinity. The

use of $FeSO_4 \cdot 7H_2O$ (FS2) resulted in significantly higher peak intensity, compared to $FeSO_4(NH_4)_2SO_4 \cdot 6H_2O$ (FS1), confirming that the choice of iron precursor is critical for successful synthesis.

The initial biomass particle size (e.g., FS2 vs. FS3; FS5 vs. FS6) and the application of an N_2 atmosphere during synthesis (FS2 vs. FS4) did not produce a visually significant effect on the Fe_3O_4 crystal structure as observed by XRD peak intensity or width. A 1:1 ratio (FS8) yielded the most intense Fe_3O_4 peaks. Increasing the biomass proportion (1:2 in FS9, 1:3 in FS10) led to a marked reduction in peak intensity, suggesting that excessive biomass hinders the successful formation or isolation of the magnetite phase.

The average crystallite size (D) for each magnetic composite (FS1–FS10) was determined using the Debye-Scherrer equation (Equation (4)).

$$D = \frac{Ks \cdot \lambda}{B \cdot \cos\theta} \quad (4)$$

In this formula, K_S represents the dimensionless shape factor (0.9), λ is the X-ray wavelength (0.15405 nm for *Cu Kα* radiation), B is the full width at half-maximum (FWHM) in radians, and θ is the Bragg diffraction angle.

The crystallite size analysis of the FS series reveals a clear distinction between the synthesis methods, with most composites falling within the true nanometric range (below 20 nm).

The use of Mohr's salt as a unique iron source in sample FS1 resulted in the largest average crystallite size of 31.21 nm. This suggests that the precursor chemistry significantly influences nucleation and growth rates, leading to more ordered and larger crystals compared to standard co-precipitation.

Samples synthesized under ambient air and nitrogen atmospheres showed varying crystallite sizes ranging from 9.61 nm to 14.52 nm. Specifically, the smallest crystallite size was recorded for FS2 (9.61 nm) under ambient air with small pore size, while the introduction of N_2 gas in FS4 facilitated slightly larger crystal growth (14.52 nm).

The integration of biochar supports (FS6 and FS7) maintained consistent crystallite sizes of 13.40 nm and 14.68 nm, respectively, indicating that the biochar matrix effectively stabilizes the iron oxide nanoparticles and prevents excessive agglomeration. Furthermore, varying the Fe:Precursor ratio (FS9 and FS10) showed a moderate increase in size from 12.88 nm to 15.07 nm as the precursor concentration increased.

The crystallite size analysis confirms the successful synthesis of magnetic nanocrystalline composites, with most samples falling within the 9.61 to 15.07 nm range. A significant outlier was observed in FS1 (Mohr's Salt), which exhibited the largest crystallite size at 31.21 nm, indicating that this specific iron precursor promotes faster crystal growth or higher crystallinity compared to standard salts.

3.2. Impact of Synthesis Parameters on Morphology

Scanning Electron Microscopy (SEM) analysis at low and high magnifications (Figure 2) was employed to investigate the surface morphology and structural characteristics of selected magnetic biochar composites (FS4, FS7, and FS8). SEM confirmed the successful formation of Fe_3O_4 nanoparticles across all synthesized composites. At high magnification, spherical-like particles, likely Fe_3O_4 nanoparticles [39], can be observed, corroborating our XRD analysis, which indicated peak broadening due to nanostructured Fe_3O_4. All samples exhibited a porous structure inherited from the carbonaceous precursor and showed a clear tendency for nanoparticle agglomeration into clusters [31].

At low magnification, the composite FS4 displayed a uniform distribution of agglomerated nanoparticles, creating a rough, porous surface (Figure 2a). High-magnification

imaging (Figure 2d) revealed that these agglomerates were composed of well-defined, spherical nanoparticles with individual sizes in the 8.79–37.41 nm range.

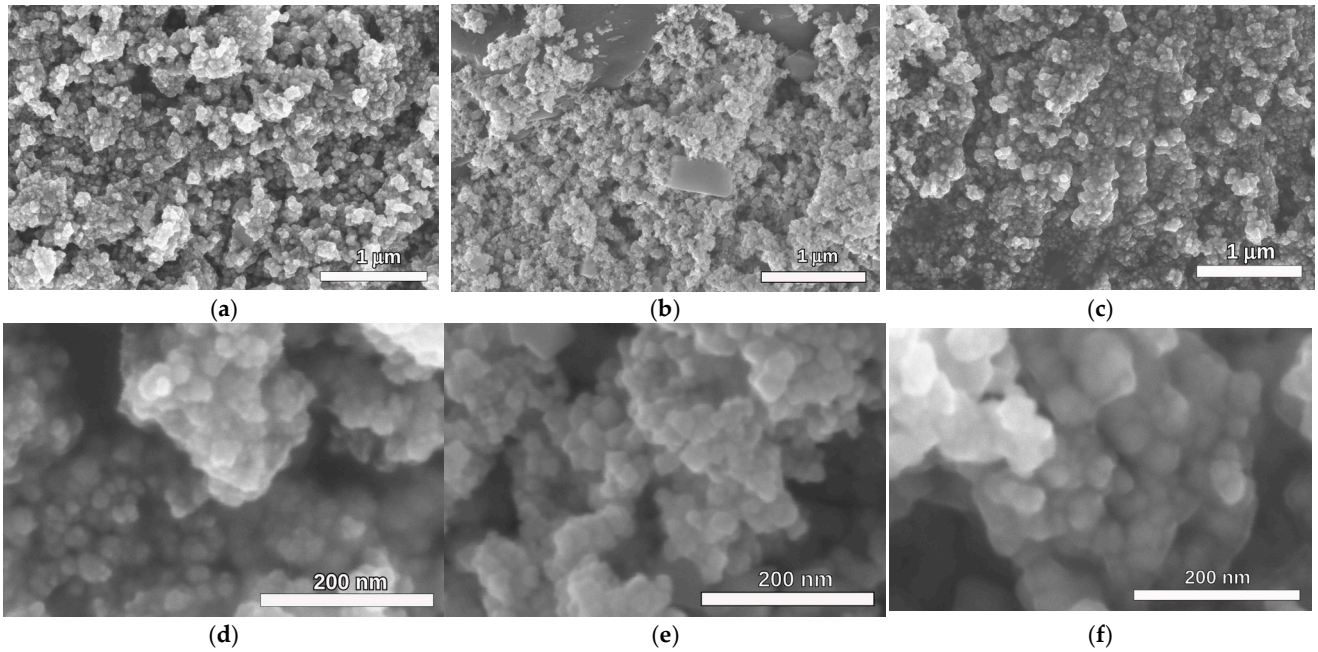

Figure 2. SEM micrographs of FS4 (**a**,**d**), FS7 (**b**,**e**), and FS8 (**c**,**f**) magnetic biochar composites at different magnifications.

The biochar-based composite FS7 showed a similar distribution of agglomerated nanoparticles (Figure 2b). The underlying matrix appeared denser and more consolidated than the biomass-based samples. The high-magnification image (Figure 2e) confirmed spherical nanoparticles of comparable size to FS4, embedded within the carbonaceous framework. The size of these nanoparticles (17.59–22.72 nm) appears to be within the nanometer range, were observed to be well-distributed and embedded within this porous carbon framework, indicating a homogeneous nanocomposite structure.

The morphology of FS8 (Figure 2c,f) was visually indistinguishable from its N_2-treated counterpart, FS4, showing similar nanoparticle size (14.31–28.58 nm), shape, and agglomeration patterns [16].

3.3. Impact of Synthesis Parameters on Textural Properties

The textural properties of the selected magnetic biochar nanocomposite (FS4, FS7, FS8), as determined by nitrogen physisorption, are summarized in Table 1. The analysis revealed that synthesis parameters significantly influenced surface area and porosity. The biochar-derived composite FS7 exhibited the most favorable textural properties, with the highest DFT surface area (31.49 m^2/g) and total pore volume (0.0801 cm^3/g). The biomass-derived composite synthesized under an N_2 atmosphere, FS4, showed intermediate values (24.28 m^2/g for surface area; 0.0739 cm^3/g for pore volume). In contrast, FS8 (biomass-based, no N_2) possessed the lowest surface area (21.74 m^2/g) and pore volume (0.0573 cm^3/g). All composites were confirmed as mesoporous, with average pore sizes ranging from 7.65 to 9.34 nm.

Table 1. Surface Area and Pore Characteristics of Fe_3O_4/Biomass (FS4, FS8) and Fe_3O_4/Biochar (FS7) Composites.

Parameter	Unit	FS4	FS7	FS8
Surface Area	m^2/g	24.28	31.49	21.74
Total Pore Volume	cm^3/g	0.0739	0.0801	0.0573
Average Pore Size	nm	9.2	9.34	7.65

3.4. Evaluation of Adsorption Performance and the Impact of Synthesis Parameters

Figure 3 presents the arsenic removal percentages for the magnetic biochar nanocomposite (FS1–FS10) compared to the raw pecan nutshell control (PM). PM demonstrated very low removal efficiency, generally below 30%, confirming that the incorporation of Fe_3O_4 is crucial for effective arsenic adsorption. This enhancement is expected, as iron oxides, particularly magnetite, are well-known for their high affinity for arsenic species [40–43].

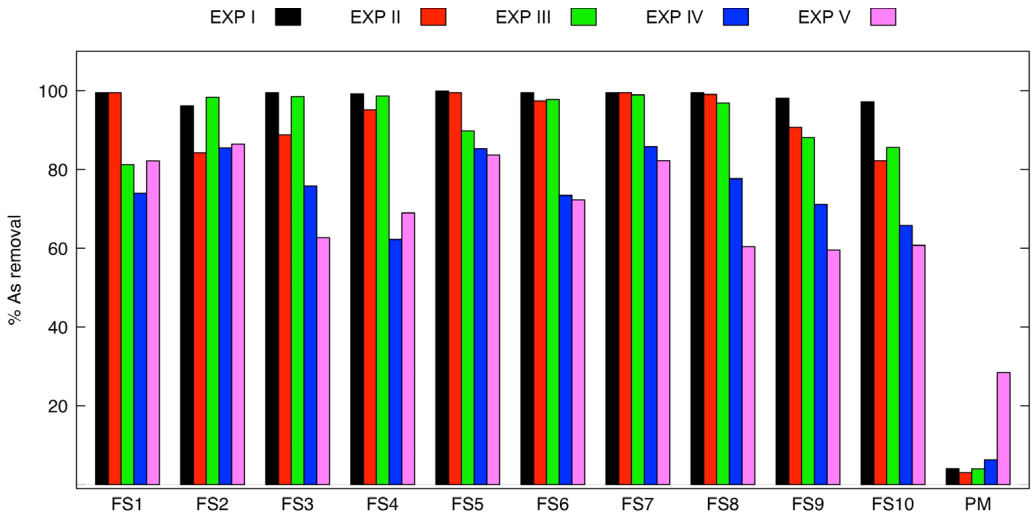

Figure 3. Arsenic removal efficiency of magnetic composites (FS1–FS10): influence of precursor, particle size, N_2 atmosphere, and Fe:precursor ratio [14].

The arsenic removal efficiency was highly dependent on the initial solution pH across the five experimental conditions [44]. In the EXP I, III, and IV (pH 3), the composites consistently achieved the highest removal rates, typically > 95%, regardless of variations in arsenic concentration (1–10 mg/L) and adsorbent dose (1–2 g/L). This research is particularly relevant to real-world conditions. It targets the acidic to neutral pH range (pH 3–5), which is most commonly found in arsenic-contaminated groundwater or industrial wastewater, thereby ensuring immediate environmental applicability. However, the study did not explore the adsorbent's performance in neutral or alkaline conditions, which may be encountered in some real-world water sources. Future research could expand the pH range to assess the adsorbent's versatility and effectiveness under varying environmental conditions. A slight reduction in removal efficiency in EXP II (pH 4) was observed compared to pH 3, but performance remained high. A notable and general decrease in removal efficiency in EXP V (pH 5) occurred for most composites at this higher pH, underscoring the importance of pH control for adsorption.

Several synthesis parameters were directly linked to the performance of arsenic adsorption. The effect of the Fe:precursor ratio was evaluated by comparing FS1, FS8, FS9, and FS10, which shared a biomass particle size of 0.18–0.38 mm. As the ratio decreased from high iron content (e.g., 1:1 in FS1, FS8) to lower iron content (e.g., 1:2 in FS9 and 1:3 in FS10), a significant decline in arsenic removal was observed. Composites with a lower

biomass proportion (higher iron loading, e.g., FS1–FS7) generally outperformed those with a higher biomass ratio (FS8–FS10).

When comparing composites synthesized from biochar (FS7) and raw biomass (FS1, FS8) at a constant particle size (0.18–0.38 mm) and Fe:precursor ratio (1:1), the biochar-derived sample (FS7) consistently exhibited higher arsenic removal, confirming the advantage of the pyrolyzed precursor. Composites synthesized with $FeCl_3 \cdot 6H_2O$ + $FeSO_4 \cdot 7H_2O$ mixture (e.g., FS2–FS10) showed excellent performance. FS1, synthesized with $FeSO_4(NH_4)_2SO_4 \cdot 6H_2O$, also demonstrated consistently high arsenic removal, though FS2–FS10 were superior overall.

In contrast, parameters such as precursor particle size and the use of an N_2 atmosphere, did not produce significant, consistent differences in arsenic removal efficiency across the tested conditions.

This research is particularly relevant to real-world conditions. It targets the acidic to near-neutral pH range, which is most commonly found in arsenic-contaminated groundwater or industrial wastewater, thereby ensuring immediate environmental applicability. However, the study did not explore the adsorbent's performance in neutral or alkaline conditions, which may be encountered in some real-world water sources. Future research could expand the pH range to assess the adsorbent's versatility and effectiveness under varying environmental conditions.

3.5. Fuzzy Logic Optimization of Adsorbent Performance Using MiFREN

Referring to the results of arsenic removal, the network architecture of the MiFREN was initially constructed, as shown in Figure 4.

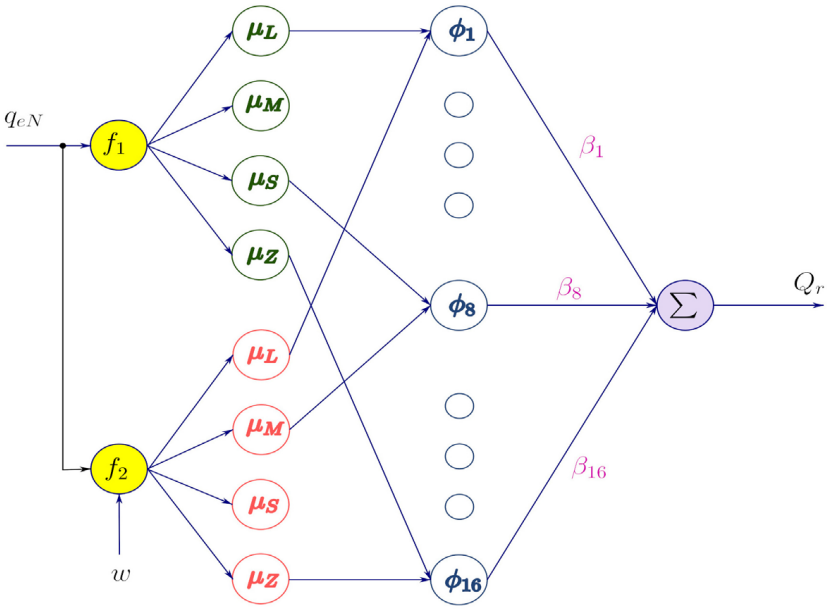

Figure 4. The network architecture of the MiFREN model utilizing normalized adsorption capacity (q_{eN}) and experimental weight vectors (w) for the assessment of arsenic removal efficiency.

The MiFREN utilized the normalized adsorption capacity, denoted as q_{eN}, as its primary input variable. This normalized metric served as a standardized measure of removal performance, allowing for consistent comparison across all experimental conditions.

The network architecture processed this input through two node functions. The second function employed a predefined weight vector, $w = [0.5, 0.6, 0.7, 0.85, 1]^T$, which was assigned to correspond with the five distinct experimental setups (EXP I–V). These weights prioritize the influence of the respective experiments, enabling the model to effectively

capture and interpret the variations in arsenic removal efficiency under different operational parameters (e.g., pH, concentration, dose).

Furthermore, the linguistic variables within the fuzzy inference system were defined by a set of membership functions, $\mu\_(L\text{-}Z)$. The design and distribution of these functions, which translated the crisp input value (q_{eN}) into fuzzy sets (e.g., "Low," "Medium," "High" removal), were graphically detailed in Figure 5. These functions were fundamental to establishing the intuitive, rule-based relationships between adsorption performance and the synthesis variables, ultimately facilitating a robust assessment and optimization of the process.

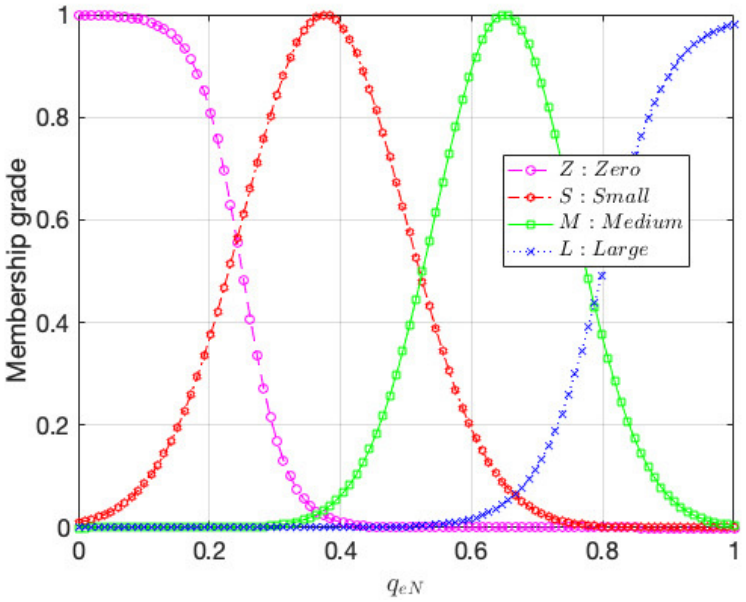

Figure 5. Architecture of the MiFREN model: input membership functions ($\mu\_(L\text{-}Z)$) for the normalized adsorption capacity (q_{eN}).

Within the MiFREN architecture, the performance index Q_r was computed as a weighted sum of fuzzy rule outputs. The quality index Q_r was determined according to the Equation (5):

$$Q_r = \sum_{j=1}^{16} \beta_j \phi_j \quad (5)$$

Here, β_j represents the weight parameter associated with the *jth* fuzzy rule. These weights are crucial as they quantify the relative importance or contribution of each specific rule to the final overall performance score. The term ϕ_j denotes the basis function for the *jth* rule. This function is the mathematical core of the fuzzy logic, calculating the degree to which a given input activates a specific rule. In this implementation, the basis function is defined as the product of two membership function evaluations: $\phi_j = \mu_L(f_1) \cdot \mu_S(w_{f2})$. This formulation allows the model to simultaneously evaluate the input against two different linguistic concepts (e.g., "Large" and "Small") that are defined by their respective membership functions μ_L and μ_S.

To streamline the model for this specific application, the functions $f_1(q_{eN})$ and $f_2(q_{eN})$ were both designated as unity functions. This was a purposeful simplification that means the input to the membership functions is the normalized adsorption capacity q_{eN} itself, without any further transformation. Consequently, the basis function ϕ_j simplifies from its general form to a more direct and computationally efficient expression: $\phi j = \mu_L(q_{eN}) \cdot \mu_S(w \cdot q_{eN})$. This simplified form retains the essential fuzzy logic operation of combining two membership evaluations while being explicitly tailored to process the q_{eN} input. Therefore, referring

to the network architecture in Figure 5, the basis functions were conducted as established in the Equations (6)–(8).

$$\phi_1 = \mu_L(q_{eN})\mu_L(wq_{eN}) \tag{6}$$

$$\phi_8 = \mu_S(q_{eN})\mu_M(wq_{eN}) \tag{7}$$

and

$$\phi_{16} = \mu_Z(q_{eN})\mu_Z(wq_{eN}) \tag{8}$$

This configuration means that the activation of each fuzzy rule is determined by comparing the measured adsorption performance (q_{eN}) against two predefined fuzzy sets, with one of the evaluations being scaled by the experiment-specific weight vector w. The weighted sum of these activations across all rules yields the final, robust performance index Q_r.

Furthermore, the nonlinear relationship between Q_r and q_{eN}, which highlights the advantage of MiFREN in capturing complex interactions, is demonstrated by the plots in Figure 6. This capability underscores the network's effectiveness in modeling intricate dependencies between variables, further validating its application in performance analysis.

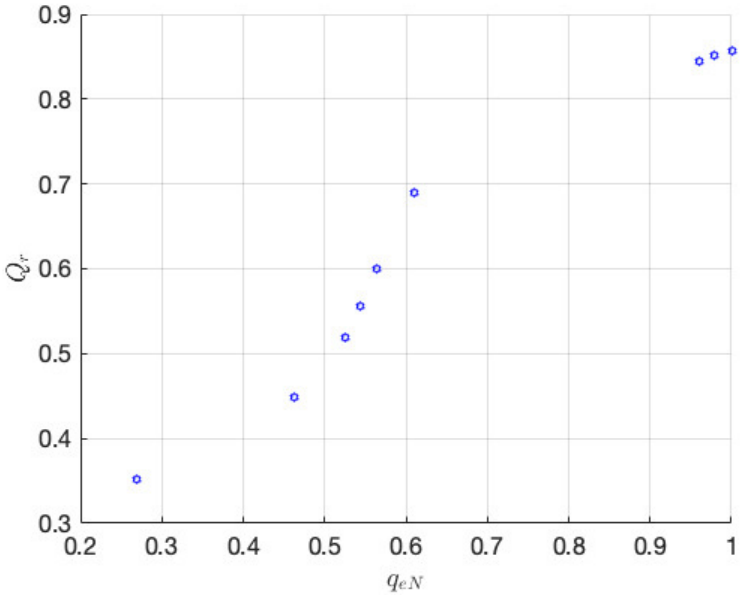

Figure 6. Nonlinear relation between performance index (Q_r) and adsorption performance (q_{eN}).

The relationship between q_{eN} and the MiFREN-derived performance index (Q_r) was presented in Figure 6. The results demonstrated a distinct nonlinear correlation between these parameters. This nonlinearity confirmed that the arsenic removal efficiency is governed by complex, interdependent relationships among the experimental variables, rather than by simple, linear dependencies.

The performance index (Q_r), derived from the MiFREN model, integrates the adsorption performance across all experimental conditions to provide a definitive ranking of the synthesized adsorbents. As shown in Figure 7, composite FS7 achieved the highest Q_r value, establishing it as the most effective adsorbent, closely followed by FS2 and FS5. The superior performance of FS2 can be attributed to its previously discussed physical structure and chemical properties. In stark contrast, FS10 registered a significantly lower Q_r value, confirming its limited effectiveness compared to other samples. These observations align with the trends in arsenic removal efficiency, emphasizing the influence of factors such as material properties, particle size, and preparation methods on the overall adsorption performance.

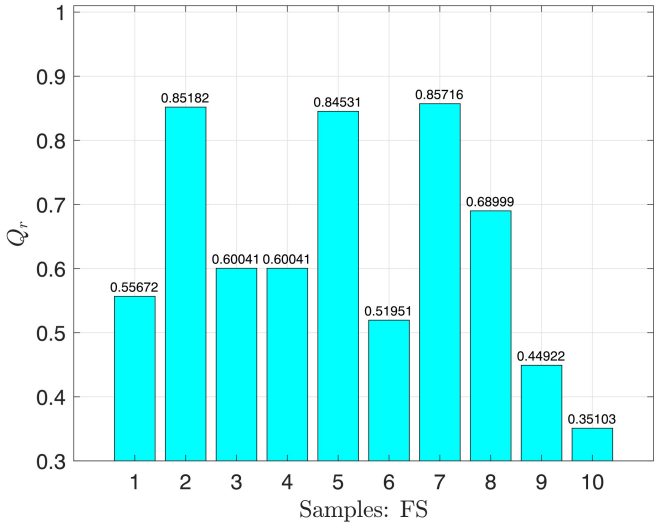

Figure 7. Ranking of adsorbent performance (FS1–FS10) for arsenic removal based on the fuzzy logic performance index (Q_r).

3.6. Kinetic Model Fitting for Arsenic Adsorption

The kinetic behavior of arsenic adsorption onto the magnetic biochar composites (FS4, FS7, and FS8) is illustrated in Figure 8. All three samples exhibited a similar two-stage adsorption profile: a rapid initial uptake occurring within the first 30–60 min, followed by a slower, gradual increase approaching equilibrium over the remaining 600 min. While the final adsorption capacities were comparable across all composites (13.0–14.0 mg/g), FS7 achieved the highest value. Regarding reaction rates, FS4 displayed the steepest initial slope, indicating the fastest uptake, whereas FS8 showed a slightly more gradual onset.

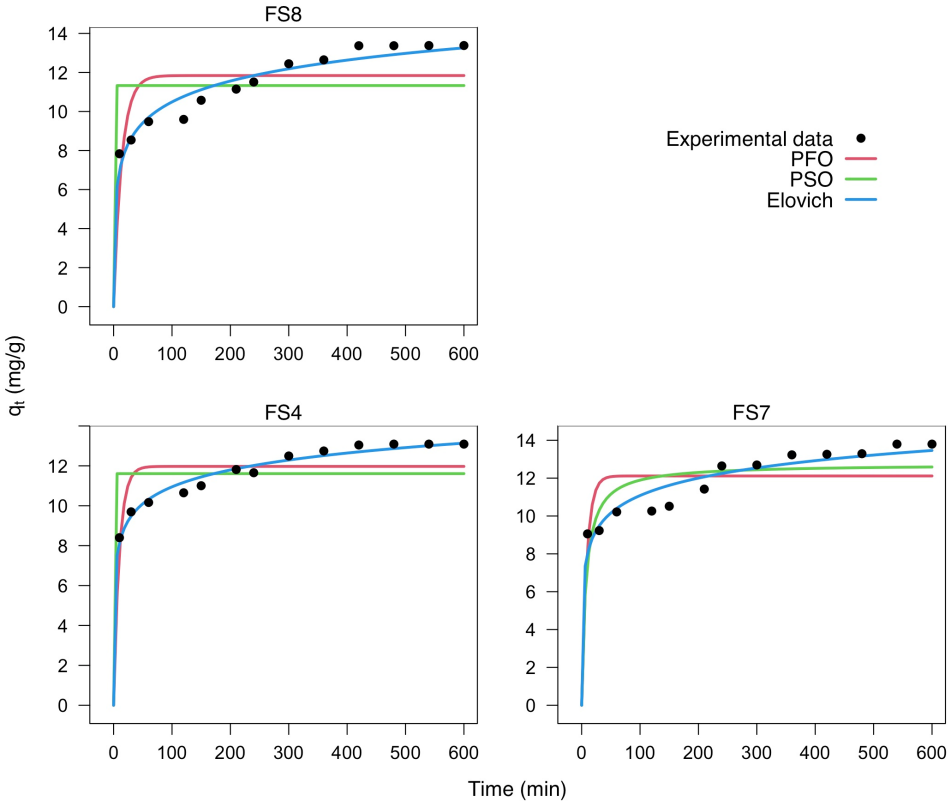

Figure 8. Adsorption kinetics of arsenic onto FS4, FS7, and FS8 fitted with Pseudo-first order, Pseudo-second order, and Elovich models.

To elucidate the adsorption mechanism, the experimental data were fitted to three kinetic models: Pseudo-First Order (PFO), Pseudo-Second Order (PSO), and the Elovich model. The calculated kinetic parameters and error analysis values (R^2 and RMSE) are summarized in Table 2. As seen in Figure 8, both PFO (red line) and PSO (green line) models predicted a premature plateau, underestimating the adsorption capacity at extended contact times. The Elovich model (blue line) provided the best fit for all three adsorbents. The R^2 values were significantly higher, ranging from 0.8708 to 0.9640, and the RMSE values were the lowest among the tested models (0.2791–0.6040 mg/g). The Elovich curve closely tracked the experimental data points throughout both the fast initial phase and the slower continuous uptake phase.

Table 2. Kinetic parameters and error analysis for the adsorption of arsenic onto FS4, FS7, and FS8.

Kinetic Model	Parameter	Unit	FS4	FS7	FS8
Pseudo-First Order (PFO)	q_e	mg/g	11.973	12.115	11.842
	k_1	1/min (or min^{-1})	0.1023	0.1145	0.0722
	R^2	-	0.4572	0.2614	0.3725
	RMSE	mg/g	1.0831	1.4441	1.5025
Pseudo-Second Order (PSO)	q_e	mg/g	12.520	12.737	12.604
	k_2	g/(mg·min) (or $mg^{-1}\cdot min^{-1}$)	0.0115	0.0111	0.0072
	R^2	-	0.7346	0.5512	0.6590
	RMSE	mg/g	0.7573	1.1258	1.1076
Elovich Model	beta (β)	g/mg	0.8178	0.7522	0.6461
	alpha (α)	mg/(g·min)	94.545	55.323	13.555
	R^2	-	0.9640	0.8708	0.9205
	RMSE	mg/g	0.2791	0.6040	0.5348

3.7. Desorption and Regeneration Studies

3.7.1. Effect of Desorbing Agents on Arsenic Recovery

The regeneration of FS7 using alkaline desorbing agents (NaOH and KOH) achieved the highest arsenic desorption efficiencies (69–96% for 0.1 M NaOH/KOH at 2–4 h). This high efficiency is attributed to hydroxide-driven disruption of Fe–O–As bonds and surface charge reversal, with 0.1 M NaOH at 4 h identified as the optimal condition [45]. While HCl showed moderate efficiency (23–32%), NaCl was largely ineffective (<4%), highlighting the dominance of pH-dependent mechanisms over ionic strength. Notably, higher concentrations (e.g., 0.2 M NaOH or 2 M KOH) did not consistently improve performance, confirming that optimal desorption occurs at 0.1 M for 2–4 h.

3.7.2. Reusability and Regeneration Cycles

The stability and performance of the FS7 composite over six consecutive adsorption–desorption cycles are presented in Figure 9.

In the first cycle, FS7 exhibited excellent remediation potential, achieving 93% arsenic removal with an adsorption capacity of 3.2 mg/g. A gradual, non-precipitous decline in performance was observed across subsequent cycles. By Cycle 3, the removal efficiency remained robust at 89%. Even by the final cycle (Cycle 6), the adsorbent retained a significant removal efficiency of 71% and a capacity of 2.0 mg/g. A sharp fluctuation was observed in Cycle 2, where the q_e value dropped to ~2.3 mg/g before recovering to ~2.7 mg/g in Cycle 3. Despite rigorous chemical processing—alternating between acidic adsorption (pH 3.0) and

strongly basic desorption (0.1 M NaOH)—the composite successfully maintained over 70% of its initial functionality after six full cycles.

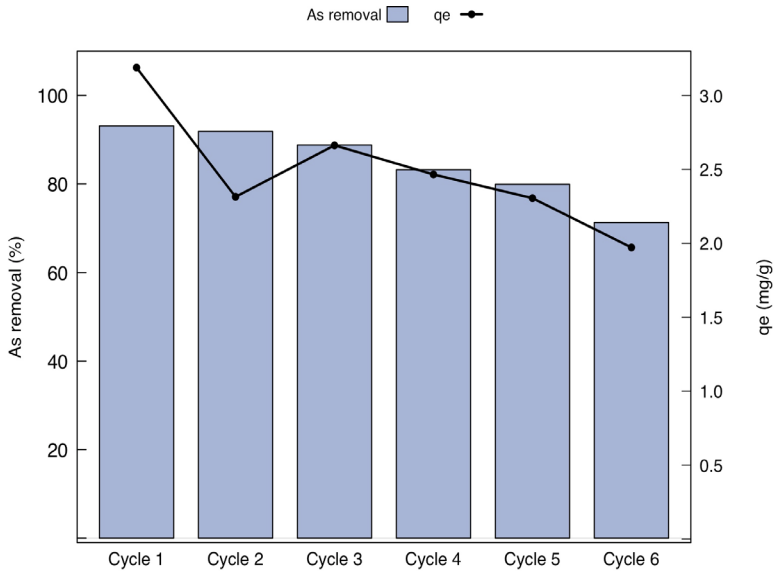

Figure 9. Reusability of the FS7 adsorbent for Arsenic removal over six consecutive adsorption–desorption cycles.

3.7.3. Structural Stability Analysis of FS7 After Desorption

Figure 10 illustrates the XRD patterns for magnetic biochar (FS7) and the material recovered after six adsorption–desorption cycles (FS7-D6). After six cycles of arsenic loading and 0.1 M NaOH regeneration, the XRD profile remained highly consistent with the pristine sample. All characteristic magnetite peaks were preserved, and no new crystalline phases (e.g., hematite or goethite) were detected. However, a slight decrease in peak intensity and a marginal increase in background noise were observed compared to the fresh material.

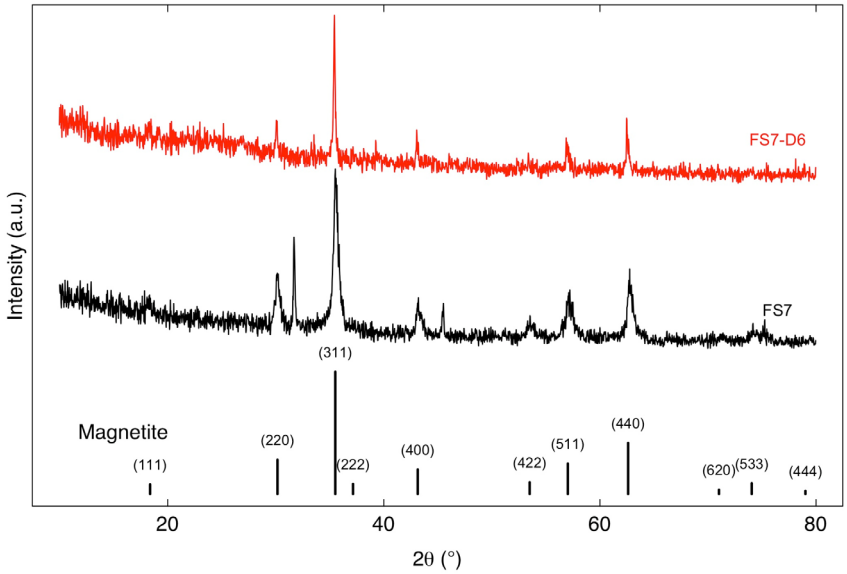

Figure 10. X-ray diffraction (XRD) patterns of the pristine FS7 nanocomposite and the regenerated material (FS7-D6) after six consecutive adsorption–desorption cycles.

3.8. Application of FS7 Nanocomposite for Arsenic Remediation in Real Groundwater

3.8.1. Groundwater Analysis and Arsenic Contamination

The groundwater from the Main Aquifer in the La Laguna Region, Mexico, presents a significant remediation challenge. Analysis reveals an initial arsenic concentration of 0.075 mg/L, which is nearly 8 times higher than the WHO and Mexican regulatory limit of 0.01 mg/L. The water is characterized by a highly alkaline pH of 11.11, low hardness (5.4 mg/L), and moderate total solids (267.0 mg/L). Major ions include Na^+, Cl^-, and SO_4^{2-}, while other heavy metals (Cd, Pb, Cr, etc.) remain below detection limits.

3.8.2. Influence of pH on Adsorption Performance

The FS7 magnetic biochar demonstrated a distinct pH-dependent performance compared to the PM adsorbent. As shown in Figure 11, FS7 reached its maximum efficiency at pH 5.0, achieving ≈ 100% arsenic removal with an adsorption capacity of 0.038 mg/g. In contrast, the PM material was significantly less effective, removing only 10% of arsenic under the same conditions.

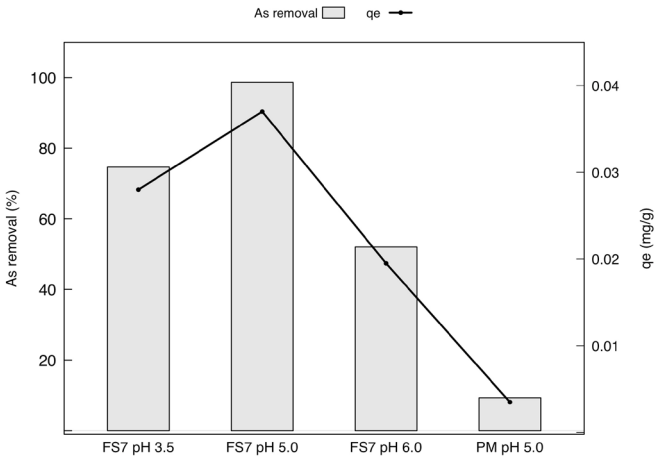

Figure 11. Effect of pH adjustment on Arsenic removal efficiency and adsorption capacity from real groundwater samples (La Laguna Region) using FS7 composite and pristine biochar (PM).

4. Discussion

4.1. Impact of Synthesis Parameters on Magnetic Phase Crystallinity

The XRD analysis provides critical insights into how the synthesis parameters influenced the formation and quality of the Fe_3O_4 magnetic phase. The results confirms that precursor type, Fe:Precursor ratio, and iron salt selection are the dominant factors controlling Fe_3O_4 crystallinity. The superior crystallinity observed in the biochar-derived sample (FS7) is attributed to the more stable and graphitic carbon matrix formed during pyrolysis. This matrix provides a superior scaffold for the nucleation and growth of well-defined Fe_3O_4 nanocrystals compared to the raw, amorphous lignocellulosic biomass [30,46]. The presence of a carbon structure from both raw biomass and biochar effectively aids in the dispersion and formation of Fe_3O_4 nanoparticles.

The standard mixture of $FeCl_3{\cdot}6H_2O$ and $FeSO_4{\cdot}7H_2O$ (used in FS2–FS10) proved more effective than the ammonium-based salt $FeSO_4(NH_4)_2SO_4{\cdot}6H_2O$ used in FS1. The distinct pattern for FS1 suggests the ammonium ions or the specific solubility limits of Mohr's salt interfered with the co-precipitation mechanism required to form the spinel structure, likely resulting in non-magnetic iron hydroxide intermediates. The $FeSO_4{\cdot}7H_2O$ promotes the formation of better-crystallized Fe_3O_4 particles [38].

Conversely, several parameters had a negligible structural impact within the tested range. Comparing samples synthesized under ambient air (FS2, FS3, FS8) with those under

N_2 protection (FS4, FS5, FS6), no significant structural difference was observed. Both sets exhibit clear characteristic magnetite peaks. This finding is significant as it suggests the co-precipitation onto the biomass matrix is robust enough to form magnetite even without an inert atmosphere. This characteristic considerably enhances the industrial scalability of the process by simplifying its operational requirements. A comparison of FS2 with FS3 and FS5 with FS6 revealed that initial particle size of the biomass precursor had a negligible impact on Fe_3O_4 formation. This indicates that the co-precipitation reaction is primarily governed by solution chemistry and the chemical functionalization of the carbon matrix, rather than the solid precursor's macroscopic surface area [22].

In this study, synthesis variations directly influenced the crystallite size, which is consistent with reported literature where crystallite sizes range from 9.9 nm in iron-manganese modified carbons [47] to 40.74 nm in leaf-derived biochars [48].

Variations in iron sources (e.g., Mohr's salt vs. standard chlorides) and Fe^{2+}/Fe^{3+} ratios are primary drivers of growth. As noted by Zhao et al. [22], these ratios determine the nucleation rate and final particle size. While pyrolysis temperature typically promotes higher crystallinity and sharper Fe_3O_4 peaks [48], our results show that at moderate temperatures, the stabilizer effect of the biochar matrix helps maintain sizes below 20 nm, preventing excessive agglomeration. The use of activation agents and specific support materials (like FS7) provides a favorable environment for the high crystallization of Fe_3O_4 without significantly increasing the crystallite size, thereby strengthening the bond between the magnetic phase and the carbon matrix [49].

Therefore, the precise control of the precursor type, Fe:Precursor ratio, and iron salt selection is essential for creating a nanocomposite with a highly crystalline magnetic phase, which directly enhances adsorption performance. The peak broadening observed across successful composites (FS2–FS10) is typical for nanoparticle systems, where the limited crystal growth is attributed to the dispersion of iron nuclei on the rough, amorphous surface of the pecan nutshell precursor [36,37].

4.2. Impact of Synthesis Parameters on Morphology

The observed spherical Fe_3O_4 nanoparticles have been observed and characterized through high-resolution imaging (Figure 2), revealing the nanoscale morphology and structural transformations, with sizes in a similar range to those found in previous studies [22,39,50]. The most significant morphological distinction arises from the precursor type. The raw biomass in FS4 and FS8 serves as a relatively amorphous scaffold, resulting in nanoparticles deposited primarily on the surface. In contrast, the pre-pyrolyzed biochar in FS7 possesses a more rigid and intrinsically porous carbon matrix [22]. This structure acts as a confining template, leading to Fe_3O_4 nanoparticles that appear better integrated within the matrix [51].

This integration is crucial as it can enhance stability and increase the accessibility of active sites by preventing the dense aggregation commonly seen on biomass surfaces [16]. Furthermore, the ubiquitous nanoparticle agglomeration observed across all samples is consistent with the broadened peaks in the XRD patterns, confirming that the composites are composed of nanoscale crystallites. The comparison between FS4 (with N_2) and FS8 (without N_2) reveals that the use of an inert atmosphere during synthesis has no discernible effect on the final nanoparticle morphology, size, or degree of agglomeration [52]. This finding aligns with the XRD result, reinforcing the conclusion that the N_2 atmosphere plays a minimal role in defining the physical and crystalline properties of the Fe_3O_4 nanoparticles under these specific synthesis conditions.

In conclusion, while the fundamental chemistry of Fe_3O_4 formation is consistent across samples, precursor is the paramount factor in engineering a superior composite

morphology, with biochar yielding a more advanced and potentially higher-performing adsorbent structure.

4.3. Impact of Synthesis Parameters on Textural Properties

The superior surface area and pore volume of FS7 compared to FS4 and FS8 are direct consequences of utilizing a biochar precursor. The pyrolysis process creates a rigid, carbonaceous scaffold that serves as an effective template for dispersing Fe_3O_4 nanoparticles and preventing dense agglomeration—a finding consistent with SEM observations. While the nitrogen environment used for FS4 also helped mitigate pore collapse compared to the oxidative environment of FS8, FS7 remains the most texturally developed composite in this study. However, it is important to note that the specific surface area (SSA) of FS7 (31.49 m^2/g) is lower than that of many pristine, non-modified biochars. This reduction is a well-documented result of pore blockage and surface coverage by Fe_3O_4 nanoparticles during the magnetization process [16,47]. Despite this relative reduction in physical porosity, FS7 maintains a competitive arsenic adsorption capacity of 12.74 mg/g. This performance indicates that arsenic removal on these magnetic composites is primarily governed by chemical sorption and surface complexation with iron-related functional groups rather than traditional physical adsorption [53]. In this context, the introduction of reactive metal sites outweighs the limitation of physical surface area. This mechanism is consistent with recent literature, where magnetic adsorbents with similar SSA ranges (13–40 m^2/g) have demonstrated effective contaminant sequestration through chemical affinity [54]. Consequently, the enhanced textural properties of FS7 facilitate the accessibility of these chemical sites, providing a synergistic effect that explains its superior performance over FS4 and FS8.

4.4. Evaluation of Adsorption Performance and the Impact of Synthesis Parameters

The stark performance contrast between the composites and the raw precursor material unequivocally identifies Fe_3O_4 nanoparticles as the primary active sites for arsenic adsorption.

The pH-dependent behavior is characteristic of As(V) removal. The maximum efficiency performance at pH 3 is attributed to the protonation of surface hydroxyl groups on the Fe_3O_4, creating a positive charge that electrostatically attracts the anionic arsenate ($H_2AsO_4^-$/$HAsO_4^{2-}$) species [24,55]. As the pH increases to 5, the surface becomes less protonated, which reduces the electrostatic attraction and causes a decline in efficiency.

The consistently high performance of both biomass and biochar-derived composites suggests that while the biochar matrix enhances porosity, the presence of well-dispersed Fe_3O_4 is the dominant factor for adsorption. The Fe_3O_4 benefits from the biochar's developed porous structure and higher surface area, which facilitates stable attachment and prevents aggregation, thus enhancing the availability of active sites [24,55,56].

The superior performance of FS7 is primarily attributed to its use of biochar as the precursor, as opposed to raw biomass. Pyrolysis at 500 °C creates a more stable, porous carbon structure with a higher surface area.

The superior performance of composites with a lower Fe:precursor ratio (e.g., FS1–FS7) indicates that an appropriate iron loading is critical. Conversely, an excess of precursor (as in FS8–FS10) hinders adsorption performance. This excess likely leads to agglomeration or incomplete Fe_3O_4 coverage, effectively reducing the density of accessible active sites. A 1:1 ratio was identified as most effective under these conditions.

The minimal impact of particle size and N_2 atmosphere suggests that within the studied ranges, the surface chemistry governed by iron oxide prevails over these physical and procedural factors.

In conclusion, the adsorption performance is predominantly controlled by the synergy between solution chemistry (pH) and the density and accessibility of Fe_3O_4 active sites, which are optimally engineered through a balanced Fe:precursor ratio.

4.5. Fuzzy Logic Optimization of Adsorbent Performance Using MiFREN

The observed nonlinearity in the Q_r versus q_{eN} relationship underscores a key advantage of the MiFREN framework over conventional regression models. While traditional methods often struggle with complex, multi-parameter interactions, MiFREN successfully captures these intricate dynamics through its adaptive membership functions and fuzzy rule-based inference. This allows the model to map how subtle changes in synthesis parameters (e.g., precursor type, particle size) non-linearly amplify or diminish the final adsorption performance.

This capability is critical for optimization. The model identifies critical thresholds and synergistic effects between parameters, revealing where specific adjustments yield the most significant gains in removal efficiency. Furthermore, this robust handling of nonlinearity and uncertainty highlights MiFREN's potential for advanced process control. The framework is not merely a diagnostic tool but a foundation for developing adaptive systems for real-time monitoring and optimization in water treatment applications, ensuring sustained efficiency under varying operational conditions.

The Q_r ranking provides a robust, data-driven validation of the impact of synthesis parameters. The superior performance of FS7 is directly attributable to its biochar-based precursor. The thermal treatment during pyrolysis creates a material with an enhanced surface area and a mesoporous structure, which facilitates superior dispersion of Fe_3O_4 nanoparticles and provides more accessible active sites for arsenic binding. The high ranking of FS2 underscores the effectiveness of refined synthesis from raw biomass, likely benefiting from its favorable physical structure and chemical composition.

Conversely, the poor performance of FS10 highlights the negative consequences of a inadequate Fe:precursor ratio. An excess of biomass likely hinders the effective formation and dispersion of Fe_3O_4 nanoparticles, reducing the density of active adsorption sites [30]. This clear hierarchy confirms that precursor selection and stoichiometric balance are critical factors governing adsorption efficacy.

Furthermore, the success of the MiFREN model in generating this reliable performance index demonstrates its significant advantage over single-condition comparisons. Its ability to handle complex, multi-parameter data and output a unified performance score underscores its potential for optimization in environmental technology. This approach is not only valuable for arsenic removal but is also readily adaptable to the design and optimization of adsorbents for a wide range of environmental contaminants, paving the way for more efficient and sustainable water treatment solutions.

4.6. Adsorption Kinetics and Mechanism

The experimental data for all composites were best described by the Elovich model, evidenced by the significantly higher coefficient of determination R^2 values ranging from 0.8708 to 0.9640) and the lowest Root Mean Square Error (RMSE) values (0.2791–0.6040 mg/g) [57,58].

The PSO model plots for FS4 and FS8 exhibit a distinct step-like shape (a rapid rise followed by a horizontal plateau) that deviates significantly from the experimental data points in the later stages (100–600 min). This visual discrepancy arises because the PSO model assumes a homogeneous surface with a definitive equilibrium point. However, the experimental data shows a continuous, slow adsorption typical of heterogeneous surfaces. Consequently, the regression algorithm forces a rapid equilibration to minimize statistical

error, resulting in an unusual fit profile. This failure of the PSO model contrasted with the excellent fit of the Elovich model ($R^2 > 0.92$)

The superior fit of the Elovich model, compared to the PFO and PSO models, strongly suggests that the adsorption process involves chemisorption on a highly heterogeneous surface. The Elovich model assumes that the active sites are heterogeneous in energy, and the adsorption rate decreases exponentially as the surface coverage increases. This is strongly supported results, as the composites are Fe_3O_4 nanoparticles dispersed on a rough, porous carbon matrix (as seen in the SEM and BET analyses). The PSO model showed a moderate fit, whereas the PFO model was largely unsuitable for describing the adsorption kinetics, suggesting that the adsorption mechanism is neither limited by simple external diffusion nor fully explained by chemisorption on a homogeneous surface [59]. Furthermore, the kinetic studies for all magnetic composites (FS4, FS7, FS8) consistently revealed a two-stage adsorption profile: a rapid initial uptake followed by a slower, gradual approach to equilibrium.

The biochar-derived composite, FS7, achieved the highest final capacity ($q_e \approx 14.0$ mg/g), which aligns with its superior textural properties as determined by BET analysis. However, based on the Elovich parameter α (representing the initial adsorption rate), FS4 exhibited the fastest initial kinetics [16]. This suggests its Fe_3O_4 sites were potentially more exposed on the external surface of the raw biomass precursor compared to the more integrated structure of the biochar-based FS7. The slow second phase suggests intraparticle diffusion into the porous matrix becomes the rate-limiting step after the easily accessible external sites are saturated [16,24].

4.7. Desorption and Regeneration Studies

4.7.1. Effect of Desorbing Agents on Arsenic Recovery

Desorption increased with contact time; however, higher alkaline concentrations did not consistently improve results, potentially leading to material damage. This research confirms the regeneration potential of biochar with alkaline agents (0.1 M NaOH) for water treatment, which also emphasize the need for proper waste management and assessment of adsorbent stability. Future work should explore eco-friendly desorbents and multi-cycle regeneration.

4.7.2. Reusability and Regeneration Cycles

The ability to regenerate and reuse an adsorbent is a critical determinant of its economic viability. The results confirm that FS7 possesses high chemical stability. The use of 0.1 M NaOH as an eluting agent effectively facilitates arsenic desorption through two primary mechanisms: (1) ion exchange which OH^- ions successfully replace adsorbed $H_2AsO_4^-$ species on the iron oxide surfaces, and (2) electrostatic repulsion which the high pH environment shifts the adsorbent surface charge to negative, repelling the anionic arsenic species into the solution.

These results align with recent findings by Hamid Ali et al. (2022) [16], who reported that 0.1 M NaOH can achieve up to 96.3% desorption efficiency for As(V) in magnetic biochar systems.

The sharp drop in q_e observed during Cycle 2 can be attributed to experimental variability in the initial arsenic concentration ($C_0 = 5.566 \pm 0.405$ mg/L). Since adsorption capacity is directly proportional to the initial concentration gradient. Importantly, the recovery of the q_e value in Cycle 3 confirms that the fluctuation in Cycle 2 was an artifact of concentration variability rather than a permanent loss of active adsorbent sites or a structural collapse of the magnetite phase.

The observed reduction in removal efficiency (from ~93% to ~71%) over six cycles is consistent with similar magnetic biochar studies [60] and can be attributed to the irreversible chemisorption, physical mass loss, and/or surface degradation [61]. While some efficiency is lost, retaining > 70% removal capacity after six cycles distinguishes FS7 as a promising, cost-effective candidate for groundwater treatment.

4.7.3. Structural Stability Analysis of FS7 After Desorption

Despite repeated exposure to pH 3.0 (adsorption) and 0.1 M NaOH (desorption), the magnetite core did not dissolve or collapse. The persistence of key peaks proves the material remains structurally intact [16]. The absence of a peak at 33° confirms the material resisted oxidation into hematite or goethite throughout the oxidative stress of six cycles [62]. The minor drop in peak intensity correlates with the decrease in adsorption efficiency from ~93% to ~71%. This is attributed to surface site passivation, minor leaching, or irreversible chemical binding of arsenic [63]. The retention of the bulk crystal structure confirms that FS7 is a robust, reusable adsorbent for long-term water treatment applications.

4.8. Application of FS7 Nanocomposite for Arsenic Remediation in Real Groundwater

The superior performance of FS7 at pH 5.0 is primarily driven by the protonation of the adsorbent surface, which facilitates a strong electrostatic attraction toward dominant arsenate species like $H_2AsO_4^-$ and $HAsO_4^{2-}$ [48,55]. This adsorption relies heavily on chemisorption mechanisms, specifically surface complexation and ligand exchange with the iron oxide components Fe_3O_4, making the iron content critical for effective removal even when physical surface area is limited [53,64]. Practically, the use of FS7 offers the advantage of magnetic recovery, allowing for facile separation via an external magnetic field and preventing secondary pollution [22]. However, for successful application in the La Laguna region, a pre-treatment acidification step to pH 5.0 is mandatory to ensure the effluent meets the WHO guideline of 10 mg/L.

The presence of major ions in the La Laguna groundwater, specifically Na^+, Cl^-, and SO_4^{2-} is expected to have a negligible impact on arsenic removal. According to the competitive affinity hierarchy ($PO_4^{3-} > SO_4^{2-} > CO_3^{2-} > Cl^-$, Cl^- and SO_4^{2-}) exhibit minimal interference, often resulting in less than a 1% reduction in efficiency [65,66]. Furthermore, monovalent cations like Na^+ do not compete for iron-oxide active sites and may even slightly enhance adsorption by compressing the electrical double layer [67]. These findings confirm that FS7 maintains high selectivity for arsenic even within a complex groundwater matrix.

5. Conclusions

This study successfully developed and engineered a magnetic biochar nanocomposite derived from low-cost pecan shell agricultural waste, demonstrating its significant potential for sustainable arsenic remediation. The co-precipitation method yielded Fe_3O_4 nanoparticle–biomass and biochar composites with high arsenic affinity. Key factors influencing arsenic adsorption performance included Fe_3O_4 loading, precursor type, and the Fe:precursor ratio. Characterization (XRD, SEM, and BET) confirmed that the precursor type (biochar vs. biomass) and the Fe:precursor ratio were the most critical factors governing the material's crystallinity, morphology, and textural properties, which directly controlled adsorption performance. The Fe_3O_4 nanoparticles were the primary drivers of arsenic adsorption.

The Fuzzy Decision Network (MiFREN) approach demonstrated high efficacy in evaluating and differentiating arsenic removal efficiency across varying experimental conditions. By leveraging normalized removal quality (q_{eN}), tailored weight vectors, and fuzzified

membership functions, the MiFREN model successfully captured nonlinear interactions and yielded an interpretable performance index (Q_r). For sample differentiation, the results reveal that FS7 consistently achieved the highest performance. Conversely, the significantly lower Q_r value for FS10 indicated its limited effectiveness, which validates the sensitivity of the MiFREN model in differentiating sample performances based on synthesis parameters. Furthermore, Q_r quantified a 50.61% difference (or derivation) between the best and worst samples, which clearly demonstrates the superior capabilities of MiFREN evaluation.

The practical application of the FS7 nanocomposite demonstrated exceptional efficacy for arsenic remediation in real groundwater from the La Laguna Region, achieving ~100% As removal at pH 5.0. Regeneration studies confirmed the material's stability, with the composite retaining 71% efficiency after six consecutive cycles.

This research resulted in the formulation of crop-derived, magnetic nanocomposites, environmentally benign and readily recoverable. These adsorbent materials are a highly promising solution for the remediation of arsenic in water.

The experimental design of this study was based on the strategic evaluation of critical parameters for arsenic adsorption, selected to represent realistic operating conditions and ensure the acquisition of comparable data at equilibrium. This intentionally limited approach aimed to generate a robust, multidimensional dataset to serve as the basis for the development and validation of the MiFREN artificial intelligence model.

The innovative contribution of this work lies in this computational framework, which, once trained, is capable of predicting adsorbent performance for a wide range of untested parameters, elucidating complex nonlinear relationships between synthesis and operating conditions, and establishing a rational, AI-guided methodology for material design. Consequently, the scope and predictive power of the MiFREN model significantly transcend the limitations inherent in purely experimental optimization approaches, offering a powerful and efficient tool for the advanced development of adsorbents applied to environmental remediation.

Author Contributions: Conceptualization, S.K. and C.T.; methodology, S.K. and C.T.; software, C.T. and A.R.-R.; formal analysis, S.K., C.T., D.-E.P.-C. and A.R.-R.; investigation, S.K., V.B.-T. and C.T.; resources, L.D.J., P.G.-M., A.Z.-G., N.T. and P.P.; writing—original draft preparation, S.K. and C.T.; writing—review and editing, V.B.-T., L.D.J., P.G.-M., N.T. and P.P.; visualization, A.R.-R.; supervision, L.D.J., P.G.-M. and A.Z.-G. All authors have read and agreed to the published version of the manuscript.

Funding: This study is partially funded by National Research Council of Thailand (Contract no. N42A671047) and Chiang Mai University.

Institutional Review Board Statement: Not applicable.

Informed Consent Statement: Not applicable.

Data Availability Statement: The original contributions presented in this study are included in the article. Further inquiries can be directed to the corresponding author.

Acknowledgments: Khamkure S. acknowledges the support from "Investigadoras e Investigadores por México SECIHTI" (Project no. 7220) and Universidad Autónoma Agraria Antonio Narro (Grant 38111-425401001-2320). We are grateful to Martha E. Rivas-Aguilar for microscopy; Sergio Rodríguez-Arias and Felix Ortega-Celaya for XRD analysis; and José Martín Baas-López, Socorro Garcia-Guillermo, Ana E. Muñez-Guajardo, J. Alejandro Espinosa-Muñoz, and M. Socorro Mireles for their assistance with chemical analysis.

Conflicts of Interest: The authors declare no conflicts of interest.

References

1. Guo, J.; Cao, W.; Lang, G.; Sun, Q.; Nan, T.; Li, X.; Ren, Y.; Li, Z. Worldwide Distribution, Health Risk, Treatment Technology, and Development Tendency of Geogenic High-Arsenic Groundwater. *Water* **2024**, *16*, 478. [CrossRef]
2. Zhang, X.; Li, Y.; He, Y.; Kong, D.; Klein, B.; Yin, S.; Zhao, H. Preparation of Magnetic Activated Carbon by Activation and Modification of Char Derived from Co-Pyrolysis of Lignite and Biomass and Its Adsorption of Heavy-Metal-Containing Wastewater. *Minerals* **2022**, *12*, 665. [CrossRef]
3. Vani, B.; Hymavathi, M.; Kalyani, S.; Sahu, N.; Sridhar, S. Effective Removal of Fluoride and Arsenic from Groundwater via Integrated Biosorption and Membrane Ultrafiltration. *Water Sci. Eng.* **2025**, *18*, 30–40. [CrossRef]
4. Bhat, A.; Ravi, K.; Tian, F.; Singh, B. Arsenic Contamination Needs Serious Attention: An Opinion and Global Scenario. *Pollutants* **2024**, *4*, 196–211. [CrossRef]
5. Jagadeesh, N.; Sundaram, B. Adsorption of Pollutants from Wastewater by Biochar: A Review. *J. Hazard. Mater. Adv.* **2023**, *9*, 100226. [CrossRef]
6. Zeng, Y.; Lin, Y.; Ma, M.; Chen, H. A Review on the Removal of Heavy Metals from Water by Phosphorus-Enriched Biochar. *Minerals* **2024**, *14*, 61. [CrossRef]
7. Fdez-Sanromán, A.; Pazos, M.; Rosales, E.; Sanromán, M.A. Unravelling the Environmental Application of Biochar as Low-Cost Biosorbent: A Review. *Appl. Sci.* **2020**, *10*, 7810. [CrossRef]
8. Vigneswararajah, V.; Thavarajah, N.; Fernando, X. Synthesis of Pectin Hydrogels from Grapefruit Peel for the Adsorption of Heavy Metals from Water. *Technologies* **2025**, *13*, 403. [CrossRef]
9. Papadaki, M.I.; Mendoza-Castillo, D.I.; Reynel-Avila, H.E.; Bonilla-Petriciolet, A.; Georgopoulos, S. Nut Shells as Adsorbents of Pollutants: Research and Perspectives. *Front. Chem. Eng.* **2021**, *3*, 640983. [CrossRef]
10. Qiu, B.; Tao, X.; Wang, H.; Li, W.; Ding, X.; Chu, H. Biochar as a Low-Cost Adsorbent for Aqueous Heavy Metal Removal: A Review. *J. Anal. Appl. Pyrolysis* **2021**, *155*, 105081. [CrossRef]
11. Inyang, M.I.; Gao, B.; Yao, Y.; Xue, Y.; Zimmerman, A.; Mosa, A.; Pullammanappallil, P.; Ok, Y.S.; Cao, X. A Review of Biochar as a Low-Cost Adsorbent for Aqueous Heavy Metal Removal. *Crit. Rev. Environ. Sci. Technol.* **2016**, *46*, 406–433. [CrossRef]
12. Amalina, F.; Razak, A.S.A.; Krishnan, S.; Sulaiman, H.; Zularisam, A.W.; Nasrullah, M. Biochar Production Techniques Utilizing Biomass Waste-Derived Materials and Environmental Applications—A Review. *J. Hazard. Mater. Adv.* **2022**, *7*, 100134. [CrossRef]
13. Thao, N.T.T.; Nguyen, D.H.; Kien, P.T.; Duong, T.-T.; Lien, N.T.K.; Tri, D.Q.; Linh, D.T.T.; Lan, N.T. Effect of Magnetic Magnetite (Fe_3O_4) Nanoparticle Size on Arsenic (V) Removal from Water. *J. Nanosci. Nanotechnol.* **2021**, *21*, 2576–2581. [CrossRef] [PubMed]
14. Khamkure, S.; Treesatayapun, C.; Bustos-Terrones, V.; Díaz-Jimenéz, L.; Pacheco-Catalán, D.-E.; Reyes-Rosas, A.; Gamero-Melo, P.; Zermeño-González, A. Fe_3O_4 Magnetic Biochar Derived from Pecan Nutshell for Arsenic Removal Performance Analysis Based on Fuzzy Decision Network. *Eng. Proc.* **2025**, *107*, 47. [CrossRef]
15. Corona-Martinez, D.-A.; Díaz-Jiménez, L.; Reyes-Rosas, A.; Zermeño-González, A.; Samaniego-Moreno, L.; Khamkure, S. Solvothermal Synthesis of Nanomagnetite-Coated Biochar for Efficient Arsenic and Fluoride Adsorption. *Eng. Proc.* **2025**, *87*, 67. [CrossRef]
16. Ali, H.; Ahmed, S.; Hsini, A.; Kizito, S.; Naciri, Y.; Djellabi, R.; Abid, M.; Raza, W.; Hassan, N.; Saif Ur Rehman, M.; et al. Efficiency of a Novel Nitrogen-Doped Fe_3O_4 Impregnated Biochar (N/Fe_3O_4@BC) for Arsenic (III and V) Removal from Aqueous Solution: Insight into Mechanistic Understanding and Reusability Potential. *Arab. J. Chem.* **2022**, *15*, 104209. [CrossRef]
17. Abbasi, M.; Rizvi, O.S.; Kajjumba, G.W.; Javed, A.; Khan, E.; Tahir, O.; Saleem, R.S.Z.; Abbas, T. Modified Biochar for Lead Removal from Water: A Critical Review on Synthesis, Characterization, Evaluation, and Unveiling the Adsorption Mechanisms Through Molecular Simulations. *Rev. Environ. Contam. Toxicol.* **2025**, *263*, 8. [CrossRef]
18. Kubar, G.M.; Kubar, A.A.; Kubar, K.A.; Shahzad, K. Biochar-Based Water Remediation: A Machine Learning Approach to Antibiotic Adsorption Prediction. *Water Air Soil Pollut.* **2025**, *236*, 898. [CrossRef]
19. Lu, X.; Han, Y.; Wang, L.; Chen, H.; Feng, Y.; Chen, Y.; Feng, Y.; Xue, L.H. Machine Learning-Driven Optimization of Metal-Modified Biochar for Phosphorus Adsorption and Wastewater Remediation. *J. Environ. Chem. Eng.* **2025**, *13*, 118839. [CrossRef]
20. Zeng, Z.; Wu, Y.; Li, W.; Han, L.; Zhao, H.; Teng, R.; Yuan, H.; Wang, Z.; Li, S.; Zeng, Z.; et al. Comparative Analysis of Multiple Machine Learning Models: Identifying Impact Factors in Biochar Heavy Metal Adsorption Mechanisms. *Environ. Geochem. Health* **2025**, *47*, 421. [CrossRef]
21. Ge, Y.; Ying, K.; Yu, G.; Ali, M.U.; Idris, A.M.; Shahab, A.; Ullah, H. A Systematic Review on Machine Learning-Aided Design of Engineered Biochar for Soil and Water Contaminant Removal. *Front. Soil Sci.* **2025**, *5*, 1623083. [CrossRef] [PubMed]
22. Zhao, Q.; Xu, T.; Song, X.; Nie, S.; Choi, S.E.; Si, C. Preparation and Application in Water Treatment of Magnetic Biochar. *Front. Bioeng. Biotechnol.* **2021**, *9*, 769667. [CrossRef] [PubMed]
23. Gupta, M.; Savla, N.; Pandit, C.; Pandit, S.; Gupta, P.K.; Pant, M.; Khilari, S.; Kumar, Y.; Agarwal, D.; Nair, R.R.; et al. Use of Biomass-Derived Biochar in Wastewater Treatment and Power Production: A Promising Solution for a Sustainable Environment. *Sci. Total Environ.* **2022**, *825*, 153892. [CrossRef] [PubMed]

24. Sharma, P.K.; Kumar, R.; Singh, R.K.; Sharma, P.; Ghosh, A. Review on Arsenic Removal Using Biochar-Based Materials. *Groundw. Sustain. Dev.* **2022**, *17*, 100740. [CrossRef]
25. Weerasundara, L.; Ok, Y.S.; Bundschuh, J. Selective Removal of Arsenic in Water: A Critical Review. *Environ. Pollut.* **2021**, *268*, 115668. [CrossRef]
26. Sherlala, A.I.A.; Raman, A.A.; Bello, M.M. Adsorption of Arsenic from Aqueous Solution Using Magnetic Graphene Oxide. *IOP Conf. Ser. Mater. Sci. Eng.* **2017**, *210*, 012007. [CrossRef]
27. Zhu, H.; Shi, M.; Zhang, X.; Liu, B.; Yao, D. Adsorption Kinetics of Arsenic (V) on Nanoscale Zero-Valent Iron Supported by Activated Carbon. *Nanomaterials* **2020**, *10*, 1791. [CrossRef]
28. Neisan, R.S.; Saady, N.M.C.; Bazan, C.; Zendehboudi, S. Optimization of Arsenic Removal from Water Using Novel Renewable Adsorbents Derived from Orange Peels. *Waste Manag. Bull.* **2025**, *3*, 21–35. [CrossRef]
29. Zeng, H.; Han, S.; Zhao, W.; Zeng, Y.; Liang, J.; Zheng, X.; Li, D.; Zhang, J. Efficiency and Mechanism of Iron Sludge-Derived Magnetic Adsorbent for Purifying Organic-Complexed High-Arsenic Groundwater. *J. Environ. Chem. Eng.* **2025**, *13*, 119066. [CrossRef]
30. Guel-Nájar, N.A.; Rios-Hurtado, J.C.; Muzquiz-Ramos, E.M.; Dávila-Pulido, G.I.; González-Ibarra, A.A.; Pat-Espadas, A.M. Magnetic Biochar Obtained by Chemical Coprecipitation and Pyrolysis of Corn Cob Residues: Characterization and Methylene Blue Adsorption. *Materials* **2023**, *16*, 3127. [CrossRef]
31. Silva, T.C.F.; Vergütz, L.; Pacheco, A.A.; Melo, L.F.; Renato, N.S.; Melo, L.C.A. Characterization and Application of Magnetic Biochar for the Removal of Phosphorus from Water. *An. Acad. Bras. Cienc.* **2020**, *92*, e20190440. [CrossRef] [PubMed]
32. López-Luna, J.; Ramírez-Montes, L.E.; Martinez-Vargas, S.; Martínez, A.I.; Mijangos-Ricardez, O.F.; González-Chávez, M.d.C.A.; Carrillo-González, R.; Solís-Domínguez, F.A.; Cuevas-Díaz, M.d.C.; Vázquez-Hipólito, V. Linear and Nonlinear Kinetic and Isotherm Adsorption Models for Arsenic Removal by Manganese Ferrite Nanoparticles. *SN Appl. Sci.* **2019**, *1*, 950. [CrossRef]
33. Gore, P.; Khraisheh, M.; Kandasubramanian, B. Nanofibers of Resorcinol–Formaldehyde for Effective Adsorption of As (III) Ions from Mimicked Effluents. *Environ. Sci. Pollut. Res.* **2018**, *25*, 11729–11745. [CrossRef]
34. Khamkure, S.; Garrido-Hoyos, S.E.; Gamero-Melo, P.; Reyes-Rosas, A. Synthesis and Characterization of Magnetic Xerogel Monolith as an Adsorbent for As(V) Removal from Groundwater. *Processes* **2021**, *9*, 386. [CrossRef]
35. Jakes, J.E. Mechanism for Diffusion through Secondary Cell Walls in Lignocellulosic Biomass. *J. Phys. Chem. B* **2019**, *123*, 4333–4339. [CrossRef] [PubMed]
36. Munasir; Kusumawati, R.P. Synthesis and Characterization of Fe_3O_4@rGO Composite with Wet-Mixing (Ex-Situ) Process. *J. Phys. Conf. Ser.* **2019**, *1171*, 012048. [CrossRef]
37. Sugurbekova, G.; Sugurbekov, E.; Demeuova, G.; Gabdullina, A.; Kudaibergenova, R. Structural and Magnetic Behavior of MFe2O4 Nanopowders for Water Treatment. *Key Eng. Mater.* **2024**, *974*, 83–90. [CrossRef]
38. He, K.; Sun, A.; Guo, Z.; Zheng, C.; Jin, Y.; Jiang, H.; Xiao, Y.; Li, J. Preparation of Nano Zero-Valent Iron-Doped Magnetic Biochar from Different Types of Iron Salts: Comparing Their Adsorption Capability for Sulfamethoxazole. *J. Environ. Chem. Eng.* **2025**, *13*, 119127. [CrossRef]
39. Jalali, M.H.; Shams, M.H.; Gholizadeh, H. Micromagnetic Simulation of the Effective Magnetic Permeability of Composites Containing Spherical Iron Nanoparticles. *J. Magn. Magn. Mater.* **2025**, *635*, 173613. [CrossRef]
40. Phearom, S.; Shahid, M.K.; Choi, Y. Nature of Surface Interactions among Fe_3O_4 Particles and Arsenic Species during Static and Continuous Adsorption Processes. *Groundw. Sustain. Dev.* **2022**, *18*, 100789. [CrossRef]
41. Kumar Jha, V.; Yadav, B.K.; Jha, V.K. Incorporation of Fe(Iii) into Bentonite and Study of Its As^{3+} Adsorption Properties. *Sci. World* **2023**, *16*, 38–49. [CrossRef]
42. Alam, E. Metal–Organic Frameworks (MOFs) for Arsenic Remediation: A Brief Overview of Recent Progress. *RSC Adv.* **2025**, *15*, 20281–20308. [CrossRef] [PubMed]
43. Rakibuddin, M.; Kim, H. Sol-Gel Derived Fe_3O_4 Quantum Dot Decorated Silica Composites for Effective Removal of Arsenic (III) from Water. *Mater. Chem. Phys.* **2020**, *240*, 122245. [CrossRef]
44. Sharma, G.; Verma, Y.; Lai, C.W.; Naushad, M.; Iqbal, J.; Kumar, A.; Dhiman, P. Biochar and Biosorbents Derived from Biomass for Arsenic Remediation. *Heliyon* **2024**, *10*, e36288. [CrossRef]
45. Bayuo, J.; Rwiza, M.J.; Choi, J.W.; Sillanpää, M.; Mtei, K.M. Optimization of Desorption Parameters Using Response Surface Methodology for Enhanced Recovery of Arsenic from Spent Reclaimable Activated Carbon: Eco-Friendly and Sorbent Sustainability Approach. *Ecotoxicol. Environ. Saf.* **2024**, *280*, 116550. [CrossRef]
46. Lavasani, F.S.; Khalaj, Z.; Kabirifard, H.; Monajjemi, M. Fabrication and Characterization of the Fe_3O_4@SiO_2-RGO Nanocomposite: A Catalyst for Multi-Component Reactions. *Phys. Chem. Chem. Phys.* **2022**, *25*, 2821–2829. [CrossRef]
47. Gallios, G.P.; Tolkou, A.K.; Katsoyiannis, I.A.; Stefusova, K.; Vaclavikova, M.; Deliyanni, E.A. Adsorption of Arsenate by Nano Scaled Activated Carbon Modified by Iron and Manganese Oxides. *Sustainability* **2017**, *9*, 1684. [CrossRef]
48. Juturu, R.; Vinayagam, R.; Murugesan, G.; Selvaraj, R. Synthesis and Characterization of Zn and Fe Doped Magnetic Biochar from *Acacia falcata* Leaves for Cr(VI) Adsorption. *Sci. Rep.* **2025**, *15*, 22146. [CrossRef]

49. Tian, L.; Li, H.; Chang, Z.; Liang, N.; Wu, M.; Pan, B. Biochar Modification to Enhance Arsenic Removal from Water: A Review. *Environ. Geochem. Health* **2022**, *45*, 2763–2778. [CrossRef]
50. Plascencia-Villa, G.; Ponce, A.; Collingwood, J.F.; Arellano-Jiménez, M.J.; Zhu, X.; Rogers, J.T.; Betancourt, I.; José-Yacamán, M.; Perry, G. High-Resolution Analytical Imaging and Electron Holography of Magnetite Particles in Amyloid Cores of Alzheimerâ €TM s Disease. *Sci. Rep.* **2016**, *6*, 24873. [CrossRef]
51. Zhou, W.; Mazarji, M.; Li, M.; Li, A.; Wang, Y.; Yang, Y.; Lee, J.T.E.; Rene, E.R.; Yuan, X.; Pan, J. Exploring Magnetic Nanomaterials with a Focus on Magnetic Biochar in Anaerobic Digestion: From Synthesis to Application. *Biochar* **2024**, *6*, 63. [CrossRef]
52. Qu, S.; Yuan, Y.; Yang, X.; Xu, H.; Mohamed, A.K.; Zhang, J.; Zhao, C.; Liu, L.; Wang, B.; Wang, X.; et al. Carbon Defects in Biochar Facilitated Nitrogen Doping: The Significant Role of Pyridinic Nitrogen in Peroxymonosulfate Activation and Ciprofloxacin Degradation. *Chem. Eng. J.* **2022**, *441*, 135864. [CrossRef]
53. Burbano, A.A.; Lassalle, V.L.; Horst, M.F.; Gascó, G.; Méndez, A. The Effect of Carbon Coating on the Arsenite Sorption by Magnetic Carbon Nanocomposites. *Int. J. Environ. Sci. Technol.* **2025**, *22*, 4749–4760. [CrossRef]
54. Azizzadeh, S.E.; Bariki, S.G.; Movahedirad, S. Magnetic Orange Leaf Biochar for Favipiravir Removal from Wastewater. *Sci. Rep.* **2025**, *15*, 25388. [CrossRef] [PubMed]
55. Hamid, Y.; Chen, Y.; Haris, M.; Usman, M.; Hussain, B.; Rashid, M.S.; Ahmed, T.; Noman, M.; Yang, X. Magnetic Biochar for the Remediation of Arsenic Contaminated Water: A Complete Guide of Science, Synthesis, and Solutions. *J. Environ. Chem. Eng.* **2025**, *13*, 118348. [CrossRef]
56. Hao, L.; Liu, M.; Wang, N.; Li, G. A Critical Review on Arsenic Removal from Water Using Iron-Based Adsorbents. *RSC Adv.* **2018**, *8*, 39545–39560. [CrossRef] [PubMed]
57. Mohamed, M.S.; Hozayen, W.G.; Alharbi, R.M.; Ibraheem, I.B.M. Adsorptive Recovery of Arsenic (III) Ions from Aqueous Solutions Using Dried *Chlamydomonas* sp. *Heliyon* **2022**, *8*, e12398. [CrossRef]
58. Cruz, G.J.F.; Mondal, D.; Rimaycuna, J.; Soukup, K.; Gómez, M.M.; Solis, J.L.; Lang, J. Agrowaste Derived Biochars Impregnated with ZnO for Removal of Arsenic and Lead in Water. *J. Environ. Chem. Eng.* **2020**, *8*, 103800. [CrossRef]
59. Vareda, J.P. On Validity, Physical Meaning, Mechanism Insights and Regression of Adsorption Kinetic Models. *J. Mol. Liq.* **2023**, *376*, 121416. [CrossRef]
60. Zhang, X.; Yang, X.; Xie, F.; Chen, X.; Zhang, Y.; Zhang, Q. Magnetic Biochar Prepared with *Rosa roxburghii* Residue as Adsorbents for Congo Red Removal. *Materials* **2025**, *18*, 1306. [CrossRef]
61. Chen, Y.; Mao, W.; Yang, W.; Niazi, N.K.; Wang, B.; Wu, P. A Novel Phosphate Rock-Magnetic Biochar for Pb^{2+} and Cd^{2+} Removal in Wastewater: Characterization, Performance and Mechanisms. *Environ. Technol. Innov.* **2023**, *32*, 103268. [CrossRef]
62. Santoso, U.T.; Abdullah, A.; Mujiyanti, D.R.; Ariyani, D.; Waskito, J. Room Temperature Synthesis of Magnetite Particles by an Oil Membrane Layer-Assisted Reverse Co-Precipitation Approach. *Adv. Mat. Res.* **2021**, *1162*, 41–46. [CrossRef]
63. Raval, N.P.; Kumar, M. Geogenic Arsenic Removal through Core–Shell Based Functionalized Nanoparticles: Groundwater in-Situ Treatment Perspective in the Post–COVID Anthropocene. *J. Hazard. Mater.* **2021**, *402*, 123466. [CrossRef]
64. Reynel-Ávila, H.E.; Camacho-Aguilar, K.I.; Bonilla-Petriciolet, A.; Mendoza-Castillo, D.I.; González-Ponce, H.A.; Trejo-Valencia, R. Engineered Magnetic Carbon-Based Adsorbents for the Removal of Water Priority Pollutants: An Overview. *Adsorpt. Sci. Technol.* **2021**, *2021*. [CrossRef]
65. Kirmizakis, P.; Tawabini, B.; Siddiq, O.M.; Kalderis, D.; Ntarlagiannis, D.; Soupios, P. Adsorption of Arsenic on Fe-Modified Biochar and Monitoring Using Spectral Induced Polarization. *Water* **2022**, *14*, 563. [CrossRef]
66. Rahman, M.A.; Lamb, D.; Rahman, M.M.; Bahar, M.M.; Sanderson, P. Adsorption–Desorption Behavior of Arsenate Using Single and Binary Iron-Modified Biochars: Thermodynamics and Redox Transformation. *ACS Omega* **2022**, *7*, 101–117. [CrossRef]
67. Nan, L.; Zhang, Y.; Liu, M.; Zhao, L.; Zhu, Y.; Zhang, X. Application of Magnetic Aquatic Plant Biochar for Efficient Removal of Antimony from Water: Adsorption Properties and Mechanism. *Separations* **2024**, *12*, 2. [CrossRef]